Journal of Fluids and Structures 132 (2025) 104195

Contents lists available at ScienceDirect

Journal of Fluids and Structures

journal homepage: www.elsevier.com/locate/yjfls

VIV mechanisms of a non-streamlined bridge deck equipped with traffic barriers

Bernardo Nicese [a,*], Antonino Maria Marra [b], Gianni Bartoli [a], Claudio Mannini [a]

[a] CRIACIV/ Department of Civil and Environmental Engineering, University of Florence, Via S. Marta, 3, Florence, Italy
[b] CRIACIV/Department of Architecture, University of Florence, Piazza Brunelleschi, 6, Florence, Italy

ARTICLE INFO

Keywords:
Vortex-induced vibration
Bridge decks
Wind tunnel tests
Traffic barriers
Vortex-shedding mechanisms
Impinging shear-layer instability
Kármán vortex shedding

ABSTRACT

Vortex-induced vibration (VIV) has been addressed in the literature mostly for quasi-streamlined and shallow π-deck sections, typical of long-span bridges, since the latter are particularly prone to wind-induced oscillations. In contrast, although full-scale observations demonstrate that even steel-box girder bridges, usually characterized by a shorter span length if compared to suspension and cable-stayed bridges, can experience a violent VIV response, systematic studies for these bluffer cross-section geometries are less frequent. In addition, the aerodynamic optimization of non-structural additions (barriers, screens, fairings) is rarely carried out for this bridge typology. Therefore, a wind tunnel investigation is conducted on a non-streamlined box-girder sectional model (inspired by the Volgograd Bridge, Russia) equipped with two typologies of traffic barriers giving rise to a large ratio of barrier height to deck width. A realistic range of angles of attack (from -3° to 3°) are considered, and static forces, aeroelastic vibrations and wake velocity fluctuations are measured. A large and even unexpected variability in the vibration amplitude and lock-in curve pattern is found, emphasizing the possible existence of competing excitation mechanisms. Indeed, low-porosity barriers can alter the characteristics of vortex shedding, in particular creating a cavity on the upper side of the deck, which is known to foster the impinging-shear-layer instability, as in H-shaped sections. This vortex-shedding mechanism may co-exist with Kármán-vortex shedding and may be responsible for significant anticipation of the VIV onset compared to the predictions based on the Strouhal number measured during static tests. The intensity of a secondary excitation mechanism and its interaction with the dominant mechanism strongly depend on the angle of attack and is largely responsible for profound changes in the VIV bridge response, both in terms of qualitative pattern and peak amplitude. In some cases, the tracks of these competing vortex-shedding mechanisms are even clearly visible in the VIV response curves of the tested bridge model. Finally, the wind tunnel results are also reconsidered based on the quasi-steady theory, highlighting some, even qualitative, discrepancies.

1. Introduction

The construction of light and slender bridge structures, characterized by limited mass per unit length and low frequency of oscillation, has become more and more common over the years. For this reason, the study of vortex-induced vibrations (VIV) of bridge decks can be crucial for the structural design. Such a phenomenon is able to produce remarkable oscillations, with possible fatigue

* Corresponding author at: University of Florence, Florence, Italy.
E-mail address: bernardo.nicese@unifi.it (B. Nicese).

https://doi.org/10.1016/j.jfluidstructs.2024.104195
Received 15 February 2024; Received in revised form 15 July 2024; Accepted 22 September 2024
Available online 25 November 2024
0889-9746/

List of symbols

B	upper width of the bridge section [mm]
b	lower width of the bridge section [mm]
C_D	drag coefficient
C_{Fy}	transverse force coefficient
C_L	lift coefficient
C_{L0}	dimensionless amplitude of the vortex-shedding force
D	across-flow dimension of bridge bare-deck section [mm]
F_D	drag force [N]
F_L	lift force [N]
h	height of the lateral traffic barriers [mm]
L	length of the sectional model [mm]
M	effective oscillating mass [kg]
m	effective oscillating mass per unit length [kg m^{-1}]
n^*	dimensionless frequency associated with the impinging shear-layer instability mechanism
n_0	natural frequency of the oscillating system [Hz]
$n_0{}^*$	dimensionless natural frequency of the oscillating system
n_s	vortex-shedding frequency [Hz]
Re	Reynolds number
Sc	Scruton number
St	Strouhal number
U	reduced wind velocity
U^*	theoretical critical reduced velocity associated with impinging shear-layer instability
V	wind velocity [m s^{-1}]
y	transverse displacement [mm]
y_{10}	mean value of the 10 %-highest peaks in the transverse displacement time history [mm]
α	wind angle of attack [°]
ζ_0	mechanical damping ratio of the oscillating system
ζ_{aero}	aerodynamic damping ratio
ζ_{aero}^{QS}	aerodynamic damping ratio predicted by quasi-steady theory
ρ	air density [kg m^{-3}]

damage accumulation on structural elements and travel safety and/or comfort level reduction for pedestrians and road or railway users.

The relevance of this phenomenon in bridge design is demonstrated by several well-known examples of bridges suffering from VIV, such as the Great Belt East Bridge in Denmark (both the suspension bridge deck and the access viaduct girder; Schewe and Larsen, 1998; Larsen et al., 2000; Frandsen, 2001) or the Trans-Tokyo Bay Crossing Bridge in Japan (Fujino and Yoshida, 2002). An evocative case of VIV recently affected the Volgograd Bridge, Russia, which showed large vertical vibrations in May 2010, just few months after completion, with a maximum peak-to-peak amplitude of approximately 80 cm. To suppress the wind-induced oscillations, semi-active tuned mass dampers were designed and installed inside the girder (Weber et al., 2013). Such a VIV event had a strong echo in the media and pointed out the potentially severe effects of vortex shedding not only for cable-supported decks but also for a girder bridge with shorter spans. Finally, the vortex-induced oscillations observed in May 2020, in the Humen Pearl River Bridge, in the Guangdong province in China, also deserve a mention, since this bridge had never been affected before by significant vortex-induced oscillations though it was opened in 1997. This VIV event was probably promoted by the temporary installation of water-filled barriers (Ge et al., 2022), with a consequent modification of bridge aerodynamics, and it is representative of the critical alteration of the VIV response caused by non-structural elements installed on the deck.

A large part of the literature about VIV refers to cylindrical bodies with paradigmatic and simple cross-section geometry, such as circle, square or rectangles with various side ratios. In the engineering practice, the circular section is representative of a multitude of different structural elements, like cables, chimneys or risers. On the other hand, square and rectangular sections are largely studied in the context of wind action on tall and slender buildings, suspenders, etc. Elongated rectangular sections are also considered in several studies dealing with bridge deck VIV (e.g., Ehsan and Scanlan, 1990; Matsumoto et al., 1993; Marra et al., 2011, 2015). Nevertheless, even for similar width-to-depth ratios, bridge sections exhibit a large variety of shapes, which are the result of structural and non-structural elements, both influencing the VIV response.

The VIV behavior of a bridge deck is strictly connected to the physical mechanism of vortex-excitation. In this respect, Shiraishi and Matsumoto (1983) classified rectangular and bridge sections in three groups based on their vortex-excited across-wind response. In particular, one of them refers to moderately elongated sections, with a side ratio between approximately 2 and 7.5 (see also Matsumoto et al., 1993), representative of elongated rectangular cylinders and a multitude of bridge decks. In this case, two kinds of unsteady vortices may coexist: one generated at the leading edge due to the vibration of the body, and the other shed in the wake near the trailing edge. This excitation is denoted by Matsumoto (1999) as one-shear layer-related vortices, because these vortices are not generated by the interaction of upper and lower shear layers, like for Kármán vortex shedding. This mechanism is also called motion-induced excitation by Matsumoto et al. (1993), to emphasize the fact that it is triggered by the motion of the body. It is characterized by a nondimensional frequency of about 0.6 (if normalized with the cross-section width), constant over a wide range of side ratios since the vortices travel along the cross-section side surfaces with a convection velocity equal to approximately 60 % of the free-stream velocity. The periodicity of this vortex-shedding mechanism is associated with the coalescence of the secondary vortex forming at the trailing edge of the section (Shiraishi and Matsumoto, 1983; Matsumoto, 1999). Higher modes with integer multiples of this frequency are possible if more than one vortex at a time travels along the lateral sides of the cross section. In contrast, other researchers (e.g., Rockwell and Naudascher, 1978; Nakamura and Nakashima, 1986; Nakamura et al., 1991; Naudascher and Wang, 1993) addressed this mechanism without invoking the motion of the body and called it impinging shear-layer instability, edge tone or impinging leading-edge vortex (ILEV). In their view, a single separated shear layer forms a vortex in the presence of a sharp trailing edge, following the feedback effect of it. This phenomenon is supposed to rule the shedding of vortices for rectangular cylinders with a side ratio greater than about 3, H and T-shaped cross sections, and other elongated bluff cylinders (see, e.g., Nakamura and Nakashima, 1986; Nakamura and Matsukawa, 1987; Mannini et al., 2017). According to this interpretation, the Strouhal number (also for a body at rest) is constant for a wide range of side ratios and equal to about 0.6 (if normalized with the cross-section width). The impinging shear-layer instability is particularly pronounced for an H-shaped geometry and the flow past cavities (Rockwell and Naudascher, 1978). The associated Strouhal number takes values around 0.6 (if normalized with section or cavity width) and its integer multiples, although slightly different values can be found in experiments (see, e.g., Naudascher and Wang, 1993). It is worth noting that vertical elements installed at both ends of a bridge section, such as barriers or screens, may give rise to a sort of cavity on the upper side of the deck, especially if they are characterized by a low porosity. Matsumoto et al. (1993) and Matsumoto (1999) also showed that in some cases this mechanism can coexist and compete with Kármán vortex shedding.

The side ratio and the bare deck geometry are critical factors for bridge aerodynamic and aeroelastic behavior, but it is well known that nonstructural devices with either an aerodynamic or a service purpose may also radically affect the VIV response. Such elements are always present in bridge decks in the form of lateral traffic barriers (e.g., Kubo et al., 2002; Bai et al., 2020; Yan et al., 2022), railings or parapets for pedestrians (e.g., Larsen and Wall, 2012; Hu et al., 2018), or screens to protect from wind or noise (e.g., Honda et al., 1992). All of them exhibit a non-negligible height or, in some cases, even comparable to the depth of the bare deck. Besides the height, the position where these elements are installed on the bridge section (Honda et al., 1992; Kubo et al., 2002), and even more the percentage and distribution of the openings (Yan et al., 2022) are also very important. The distribution of open and solid portions of a barrier may even be employed to mitigate vortex-induced oscillation (Bai et al., 2020). A subset of the works mentioned above (Honda et al., 1992; Kubo et al., 2002; Bai et al., 2020) also deal with the bridge VIV behavior for a certain range of wind angles of attack, since the incoming flow inclination is strictly connected to the effect of screens or barriers installed on the deck.

To provide a clearer overview of the past research about VIV of bridge decks, which may be useful not only for the present work but also as a database for future efforts, a collection of studies available in the literature is reported in Table 1. Therein, the typology of investigation is indicated, distinguishing between wind tunnel tests (WT), computational fluid dynamics simulations (CFD) and full-scale measurements (FS). The typologies of bridges and deck sections are also reported, along with the ratios of some relevant geometric quantities: B is the total width of the cross section, while b denotes the width of the horizontal part of the lower side of the deck; D is the depth of the bare deck; h is the height of the vertical barriers or screens installed on the bridge. A graphical comparison between the bridge sections collected in Table 1 is also provided in terms of ratios between cross-section dimensions (Fig. 1a) and normalized barrier height (Fig. 1b). While h/D is a measure of the relative height of the barrier for the specific bridge deck, the ratio h/B characterizes the geometry of the cavity created on the deck upper side by a pair of lateral barriers or screens; especially for a low porosity of them, this ratio may be crucial for the vortex-shedding mechanism associated with impinging shear-layer-instability (or motion-induced excitation). The peak transverse amplitude of vibration Y_{peak}, normalized with D, and the corresponding mass-damping parameter, the Scruton number (Sc), are also reported in Table 1. The Scruton number is evaluated as $Sc = 4\pi m\zeta_0/\rho BD$, where m is the mass per unit length, ζ_0 is the structural damping, and ρ is the air density. Most of the studies collected in Table 1 deal with the VIV response of elongated or quasi-streamlined bridge deck sections, typical of long-span bridges, which usually draw the attention of researchers due to their sensitivity to wind-induced excitation. Some studies dealing with π-shaped deck sections are also included in Table 1; this section typology is often adopted for cable-stayed bridges and, despite the poor aerodynamic performance (especially in the absence of fairings), it is usually characterized by a fairly large ratio of along-wind to across-wind dimensions. The lowest B/D ratios in Table 1, lower than 4, are those associated with the Rio-Niterói Bridge (Battista and Pfeil, 2000), the Deer Isle Bridge (Kumarasena et al., 1991), the approaching spans of the Great Belt East Bridge (Larsen et al., 1995; Schewe and Larsen, 1998), and the Trans-Tokyo Bay Crossing Bridge (Fujino and Yoshida, 2002). Except for the Deer Isle Bridge, which is a suspension bridge with an open section, the others are girder bridges with a non-streamlined steel box section. Their maximum span length ranges from about 200 m to 250 m, and they exhibited remarkable peak transverse amplitude of vibration, between 4 % and 10 % of D at full scale and during wind tunnel tests. A slightly larger side ratio characterizes the Volgograd Bridge, which presents a bluff trapezoidal box girder with lateral cantilevers (Corriols and Morgenthal, 2012). This case study is meaningful, since it experienced the most violent VIV event collected in Table 1, although the deck girder is characterized by the shortest span length (155 m) among those reported there. It is also worth noting that this bridge exhibits a high ratio of the barrier height to the deck depth (h/D) and width (h/B), which is expected to have an impact on the possible excitation due to impinging shear-layer instability. The analysis of Table 1 suggests that the literature lacks studies of the VIV behavior of box cross sections characterized by low side ratios and relatively high barriers, typical of girder bridges with an important span (though noticeably shorter than those of cable-supported bridges). In addition, due to the non-streamlined deck profile and the relatively limited span length, the aerodynamic performances of non-structural additions like

Table 1
Collection of VIV studies.

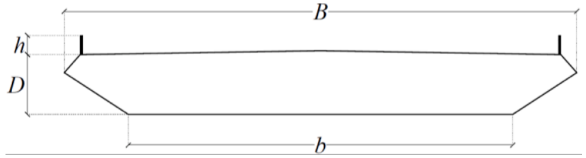

Bridge	Reference	Study	Deck section	Bridge typology	Span length [m]	B/D	b/D	h/D	h/B	St	α [°]	Y_{peak}/D	Sc
Chongqing Hechuan Bridge	Bai et al. (2020)	WT	Streamlined box girder	Suspension	400	7.6	4.1	0.4	0.05	–	−3 to 3	0.07	12.3
Deer Isle Bridge	Kumarasena et al. (1991)	FS	H-shaped section	Suspension	329	3.6	3.6	0.68	0.19	0.14	–	0.02	–
Great Belt East Bridge (suspended span)	Larsen (1993)	WT	Streamlined box girder	Suspension	1624	7	4.7	0.33	0.05	0.11–0.15*	0	0.06	–
	Frandsen (2001)	FS											
Great Belt East Bridge (approaching spans)	Larsen et al. (1995)	WT	Trapezoidal box girder	Steel girder	193	3.7	1.6	0.18	0.05	0.22	0	0.11	5.6
	Schewe and Larsen (1998)	FS									–	0.02	–
Haihe Bridge	Meng et al. (2011)	WT CFD	Trapezoidal box girder	Cable-stayed	310	8.1	4.7	0.4	0.05	0.07–0.12*	0	0.10	11.9
Hålogaland Bridge	Larsen and Wall (2012)	WT	Streamlined box girder	Suspension	1145	6.2	2.7	0.47	0.07	0.21–0.23*	0	0.04	6.2
Hong Kong-Zhuhai-Macao Bridge	Chen et al. (2017)	WT	Elongated trapezoidal box girder with lateral cantilevers	Cable-stayed	258	8.5	4.5	0.25	0.04	–	−5 to 5	0.12	7.7
Humen Bridge	Ge et al. (2022)	FS	Streamlined box girder	Suspension	888	13.3	10	0.4	0.03	–	–	0.12	13.2
Jindo Bridge – 1st bridge	Seo et al. (2013)	FS	Trapezoidal box girder	Cable-stayed	340	4.2	2.2	0.48	0.11	–	–	0.13	–
Jindo Bridge – 2nd bridge						4.8	2.3	0.46	0.10	0.11			
Jindo Bridge – parallel layout						12.7	8.1	0.47	0.04	–			
Kessock Bridge	Owen et al. (1996)	WT	Open π-shaped section	Cable-stayed	240	6.7	6.7	0.29	0.04	0.09–0.10*	0	0.05	–
Osteroy Bridge	Larsen and Wall (2012)	WT	Streamlined box girder	Suspension	595	5.4	3	0.5	0.09	0.21–0.25*	0	0.04	5.4
Qingshan Yangtze River Bridge	Li et al. (2018)	WT	Streamlined box girder	Cable-stayed	938	10.4	4.1	0.34	0.03	0.11–0.16*	−5 to 5	0.07	8.1
Rio-Niterói Bridge	Battista and Pfeil (2000)	WT	Rectangular box girder	Steel girder	300	3.5	2.7	0.19	0.05	0.12–0.18*	0	0.04	–
Second Severn Crossing Bridge	Macdonald et al. (2002)	WT	Open π-shaped section	Cable-stayed	456	10.7	6.2	0.40	0.04	0.06–0.08*	0	0.07	1.0
		FS									–	0.06	–
Stonecutters Bridge	Larose et al. (2003) Larsen et al. (2008)	WT	Streamlined twin-box girder	Cable-stayed	1018	13.6	7.2	0.40	0.03	0.20	–	0.14	–
Sunshine Skyway Bridge	Ricciardelli et al. (2002)	WT	Elongated trapezoidal box girder with lateral cantilevers	Cable-stayed	364	7.1	2.5	0.18	0.03	0.11	0	0.01	–
Tacoma Narrows Bridge	Matsumoto et al. (2003)	WT	H-shaped section	Suspension	853	4.8	4.8	0.29	0.06	0.11	0	0.27	5.0

(*continued on next page*)

Table 1 (*continued*)

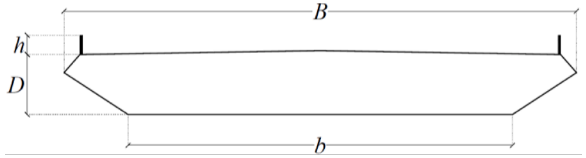

Bridge	Reference	Study	Deck section	Bridge typology	Span length [m]	B/D	b/D	h/D	h/B	St	α [°]	Y_{peak}/D	Sc
Tomei Ashigara Bridge	Honda et al. (1992)	WT	Streamlined box girder	Cable-stayed	185	8	2.8	1.3	0.16	–	−4 to 8	0.08	0.9
	Fujino and Yoshida (2002)	WT									−3 to 3	0.09	–
Trans-Tokyo Bay Crossing Bridge		FS	Rectangular box girder with lateral cantilevers	Steel girder	240	3.8	2.8	0.14	0.03	0.12–0.18*	–	0.08	–
	Sarwar and Ishihara (2010)	CFD									0	0.07	1.6
Volgograd Bridge	Corriols and Morgenthal (2012)	CFD	Trapezoidal box girder with lateral cantilevers	Steel girder	155	4.9	2	0.43	0.08	0.12	–	0.23	–
Xiangshan Harbor Bridge	Zhu et al. (2013)	WT	Streamlined box girder	Cable-stayed	688	9.1	5.3	0.42	0.05	–	0	0.09	9.1
Yi Sun-Shin Bridge	Hwang et al. (2019)	FS	Streamlined twin-box girder	Suspension	1545	10.3	4.2	0.39	0.04	0.11–0.14*	0	0.09	4.7
Generic bridge sections	Kubo et al. (2002)		Open π-shaped section			10	–	0.4	0.04	–	−6 to 6	0.15	4.7
	Larsen and Wall (2012)		Streamlined box girder			7.75	3	0.3	0.04	–	0	0.09	7.75
	Hu et al. (2018)		Streamlined box girder			10.7	6.2	0.46	0.05	0.05–0.07*	0	0.07	10
	Sun et al. (2019)	WT	Streamlined box girder	–	–	8.5	4.6	0.33	0.04	0.09	0 to 5	0.12	9.3
			Trapezoidal box girder			3.6	1.5	0.22	0.06	0.15	0 to 5	0.09	13.7
	Wang et al. (2020)		Streamlined box girder			10.5	7.2	0.52	0.05	–	0 to 7	0.05	5.6
	Yan et al. (2022)		Hexagonal box girder			5.5	3.1	0.22	0.04	0.09–0.13*	0	0.20	7.7
	Wang et al. (2023)	CFD	Streamlined box girder			13.4	10	0.34	0.02	0.04–0.06*	−3 to 3	0.37	6

[*] For the Strouhal number, a range of values deduced by the response curves is reported when the exact value is not indicated in the paper.

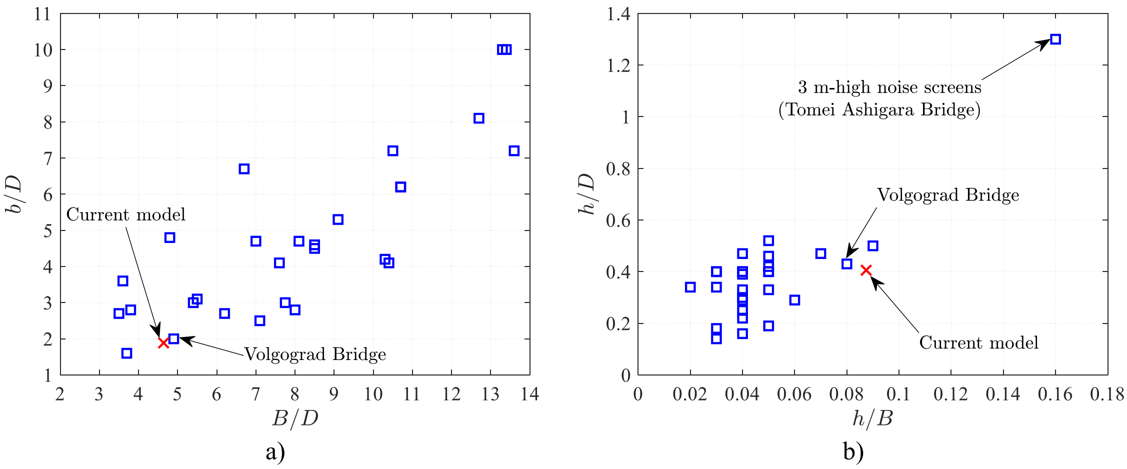

Fig. 1. Comparison between the bridge sections collected in Table 1 and the current sectional model in terms of b/D against B/D (a) and of h/D against h/B (b).

barriers or screens are frequently overlooked for this bridge typology, so that they are rarely optimized from the aerodynamic point of view. Finally, most of the collected literature contributions are limited to the null angle of attack, despite the well-known importance of this parameter.

Based on these considerations, in the present work a wide experimental campaign is performed on a sectional model presenting a realistic and relatively bluff geometry, inspired by the Volgograd Bridge deck and having large traffic barriers compared to the depth and, above all, to the width of the deck section (see Fig. 1). The aerodynamic effects of two different typologies of lateral traffic barriers are evaluated by means of static force measurements and aeroelastic tests. Wake measurements behind both the stationary and the vibrating model are also performed in some cases, to better understand the VIV response. The study is carried out over a range of angles of attack typical of practical applications. The experiments aim to shed some light on the different vortex-induced excitation mechanisms and their possible interaction or interference, which is an aspect that is usually not dealt with for bridge sections equipped with realistic additions. Attention is paid to the influence of the barriers not only on the VIV response amplitude but also on the onset and extension of the lock-in regime, always keeping in mind literature results for more generic and paradigmatic cross sections (e.g., rectangular and H-shaped sections). The accuracy of the quasi-steady theory in predicting potential galloping instabilities of the considered bridge model is also ascertained. From a practical engineering perspective, the current work also aims at warning practitioners about the complex and problematic wind-induced behavior girder bridges can exhibit in some cases, especially when low-porosity barriers are installed or if non-null angles of attack can be expected.

2. Wind tunnel experiments

2.1. Wind tunnel facility and model

The tests are carried out in the open-circuit boundary layer wind tunnel of CRIACIV (Inter-University Research Centre on Building Aerodynamics and Wind Engineering), located in Prato, Italy. The closed rectangular test section is 2.42 m wide and 1.60 m high. The flow is drawn by a 156-kW fan, and its speed can be continuously varied in the range $0 - 30$ m s^{-1}, with a free-stream turbulence intensity below 1 %. Temperature and atmospheric pressure are constantly monitored with a probe to calculate the air density.

A bridge deck sectional model is employed for both static and aeroelastic tests, with a cross section inspired by the Volgograd Bridge, in Russia. This bridge is characterized by a slightly non-symmetric cross section, with two lateral cantilevers of different lengths

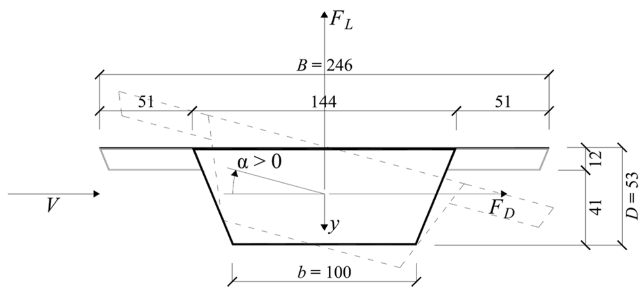

Fig. 2. Sketch of the sectional model cross section (dimensions in mm). Positive drag, lift and angle of attack are also indicated.

jutting out from a trapezoidal steel box girder (Corriols and Morgenthal, 2012). Such a length difference comes from the presence of a walkway only on one of the two sides of the section. In contrast, the cross section of the wind tunnel model is symmetric, aiming at a more paradigmatic deck geometry and, hence, at a greater generality of the work.

Fig. 2 shows a schematic representation of the model cross section. F_D and F_L denote respectively the drag and lift forces, V is the wind velocity, and α is the angle of attack (positive nose up). The sectional model is 1000 mm long (L), its upper and lower widths are respectively 246 mm (B) and 100 mm (b), while the across-flow size is 53 mm (D), referring to the bare deck layout. The resulting cross-section side ratios are $B/D = 4.6$ and $b/D = 1.9$. The box girder is realized with a 1 mm-thick aluminum plate, and a 0.5 mm-thick upper horizontal plate is fixed on the top of the girder, supported by lateral ribs on both sides. Internal ribs in the trapezoidal core of the model are also employed to avoid model deformation. The model lower corners are made sharp using a two-component adhesive paste (Fig. 3a). To promote two-dimensional flow conditions, aluminum rectangular end-plates (500 mm × 210 mm, having a thickness of 2 mm for the static tests and 1 mm for the dynamic tests) are provided at both ends of the model. Including the light end-plates, the model has a mass of 2.81 kg.

Two realistic typologies of bridge lateral barriers are installed on the model (Fig. 3b-e). They are made of aluminum and present nearly the same height but a different degree of porosity: the first one (Barrier 1) is 21 mm high, while the second one (Barrier 2) is 22 mm high; their porosity is 51 % and 23 %, respectively. The largest blockage ratio (conservatively calculated as the total depth of the model in the direction perpendicular to the wind divided by the height of the test chamber) is 6.8 %, obtained during static force measurements for the model equipped with barriers at an angle of attack of about 12° Nevertheless, most of the tests discussed in the present paper refer to an angle of attack ranging between −3° and 3°, and in these cases the maximum blockage ratio is equal to 5.3 %, which is generally considered acceptable.

Finally, it is worth remarking that Barrier 1 is quite similar to the one installed on the Volgograd Bridge on the side opposite the walkway. On the other hand, Barrier 2 is representative of partially solid traffic barriers employed to increase the safety of motor-cyclists on the road, especially when cornering. It may also be representative of other cases in which weakly porous vertical elements or solid elements up to a considerable height are installed on the deck. For example, such a geometric condition may occur for pedestrian parapets made of glass or similar materials.

2.2. Experimental setups

Static force measurements are performed by rigidly connecting the sectional model at both ends to two ATI FT-Delta SI-165–15 six-component high-frequency force balances (Fig. 4(a)). Each balance is fixed to an electric motor allowing the automatic rotation of the

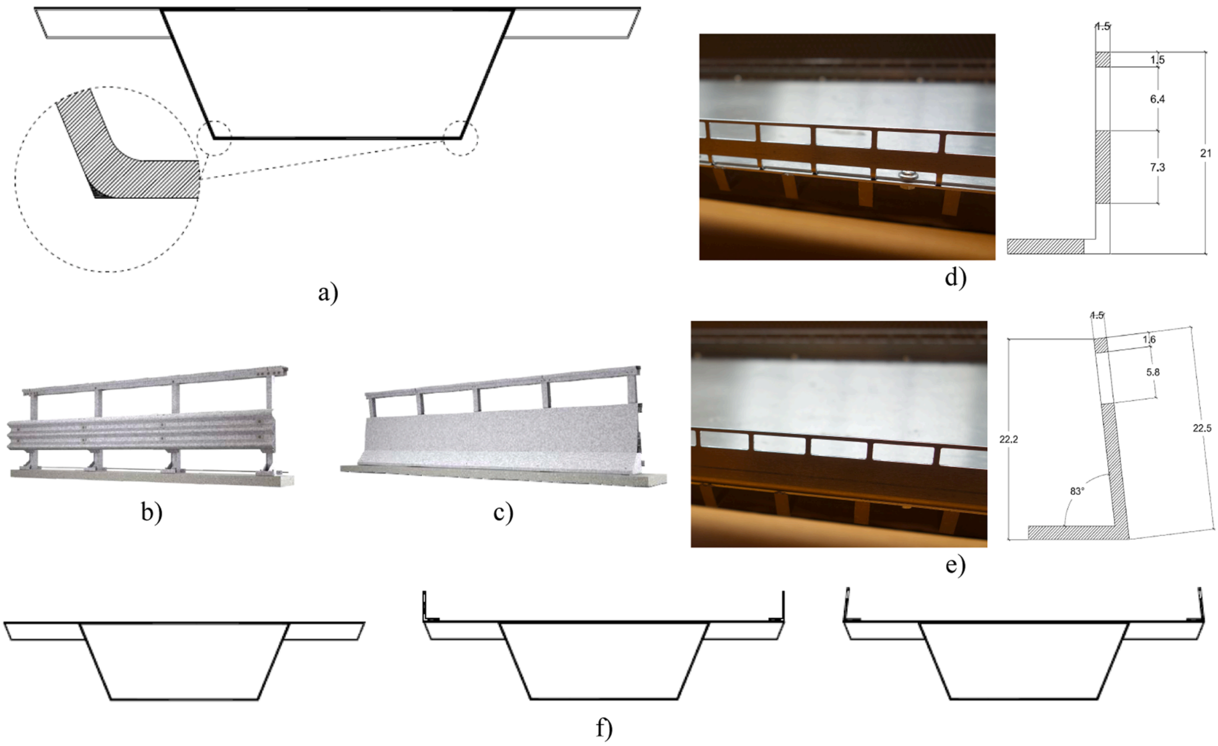

Fig. 3. Lower corner shape variation (a), Barrier 1 (b) and Barrier 2 (c). Close-up and main dimensions (in mm) of the first (d) and the second (e) lateral barrier installed on the sectional model during the tests. Section layouts without barriers (left), with Barrier 1 (center) and with Barrier 2 (right) are also reported (f).

sectional model around its longitudinal axis, to vary accurately the value of the angle of attack. The whole mechanism is supported by two steel columns fixed to the floor of the wind tunnel. The natural frequency of the system composed by the model installed on the setup for static force measurements is about 25 Hz.

Aeroelastic tests are conducted by elastically suspending the model through two shear-type steel frames, connected to the longitudinal axis of the model (Fig. 4(b)). The horizontal elements of the frames work as leaf springs. Only the vertical transverse displacement of the model is allowed, because of the very high in-plane bending stiffness of the vertical Vierendeel-type girder welded to the horizontal plates and rigidly connected to the sectional model. The displacements of the sectional model are recorded with two non-contact laser transducers Micro-epsilon OptoNCDT 1605, placed below both ends of the model. The mechanical damping of the system is varied through a device based on the electromagnetic induction principle. It consists of two thin aluminum plates (250 mm × 120 mm × 2 mm), each one fixed to the end of a leaf spring and moving between two pairs of magnetic disks with a diameter of 60 mm and a thickness of 5 mm (Fig. 4(b)). The development of eddy currents in the aluminum plates generates a viscous damping force in the oscillating system. The amount of damping is controlled by finely tuning the distance between the magnets. The frequency (n_0) and the mechanical damping ratio (ζ_0) of the oscillating system are measured through free-decay tests.

Dynamic system identification is repeated several times for each series of aeroelastic measurements, showing very good repeatability. Damping is identified through the MULS method (Bartoli et al., 2009; see Fig. 5(a, b)) over time windows varying from 5 s for the lowest amplitudes to 2 s for the largest amplitudes (i.e., for approximately 15 to 45 oscillation cycles) and is associated with the maximum displacement in the window. Fig. 5(c) and 5(d) compare the results of three identifications for two different values of the mechanical damping of the system. When the damping is very low (significantly below 0.1 % in Fig. 5(c)), increasing the oscillation amplitude by a factor of 10 causes a growth in the damping ratio by more than a factor of two, mainly due to the still-air resistance. In fact, the damping value tends to stabilize for very low oscillation amplitudes. Conversely, the amplitude-dependence of damping is less pronounced for a larger value of the mechanical damping (about 1.2 % in Fig. 5(d)), due to the very good linearity of the dissipation force produced by the eddy-current dampers and the reduced relative importance of still-air resistance. In general, since the effect of still-air resistance does not linearly superpose to that of the airflow, aiming at minimizing its effect and estimating the damping value corresponding to incipient instabilities, in the remainder of the paper we will always refer to the damping values determined for small oscillation amplitudes (below 0.5 mm, that is below about $0.01D$), bearing in mind, however, that there is some uncertainty in the estimation of this important set-up parameter.

The effective mass of the oscillating system (M) is evaluated through the addition to the system of a set of known masses and the consequent identification of vibration frequencies. An effective mass of 5.9 kg is estimated for the bridge deck sectional model (excluding the aluminum plates of the dampers and the lateral barriers installed on the bridge deck model). This result is confirmed by the direct measurement of the stiffness of the system (17.4 kN/m). Furthermore, the linear elastic behavior of the leaf springs is verified up to the highest amplitudes observed during the experimental tests. The natural frequency of the vibrating system ranges from 8 to 9 Hz, while the Scruton number, calculated as $Sc = 4\pi M\zeta_0/\rho BDL$ (where ζ_0 refers to the damping in still air for small oscillation amplitude), varies from about 3.5 to about 60.

Finally, flow-velocity measurements are performed through a hot-wire anemometer installed on a robotic arm, able to move in all directions inside the test chamber behind the sectional model. The measurements are carried out with the model mounted on the aeroelastic setup (Fig. 4(b)) and they are performed both in static and dynamic conditions. In particular, for the former, the two shear-type steel frames supporting the model are restrained by a diagonal aluminum element inside the frame and by a cable connected to the floor of the wind tunnel, preventing any vibration of the system. Fig. 6 provides the layout of the setup for the wake measurements; the probe is placed in two different positions, either at a distance of $2.9D$ downstream of the model (position P1) or much closer to the leeward barrier, at a distance of $0.75D$ from it (position P2). In both cases, the probe is located about $0.85D$ above the upper side of the deck.

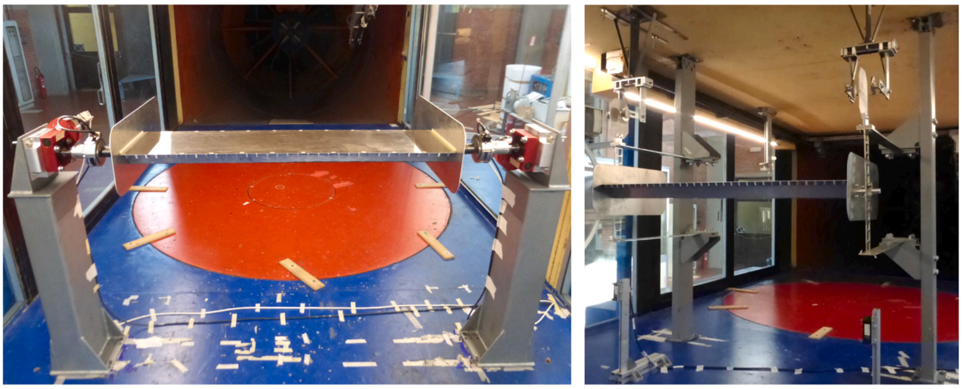

a) b)

Fig. 4. Wind tunnel setup for static force measurements (a) and aeroelastic tests (b).

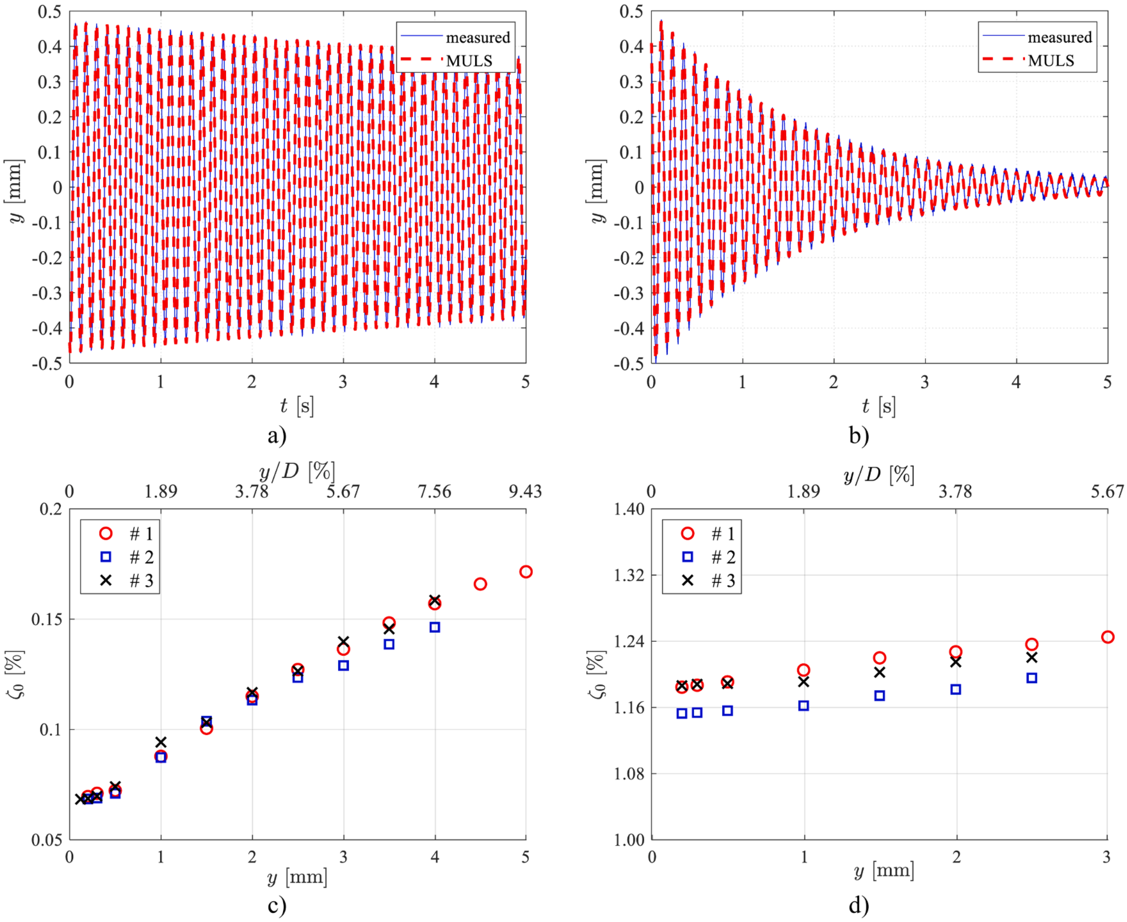

Fig. 5. Comparison between the transverse displacement signal measured during free-decay tests in still air and the associated signal reconstructed through the MULS method (a, b). Comparison of three repetitions of damping-ratio identification tests for different values of the initial oscillation amplitude (denoted as y) (c, d). The left frames (a, c) refer to the system with very low damping, while the right frames (b, d) correspond to the system with higher damping due to the activation of eddy-current devices.

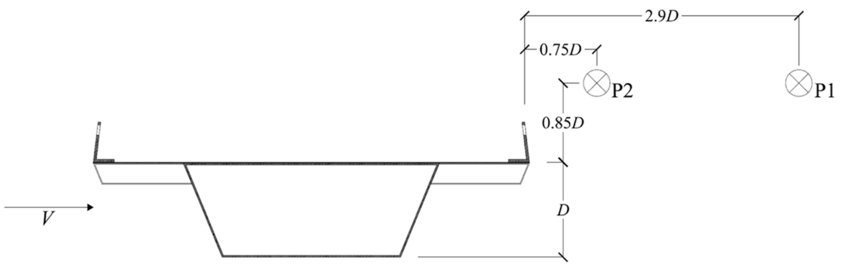

Fig. 6. Sketch of the bridge deck sectional model with the indication of the positions P1 and P2, where the hot-wire probe is placed to perform wake measurements.

3. Results

3.1. Static force measurements

The static force measurements are carried out to describe the aerodynamic behavior of the bridge deck section and support the discussion of the VIV response in the aeroelastic tests. First, the mean values of drag (F_D) and lift (F_L) forces are measured. Aerodynamic drag (C_D) and lift coefficient (C_L) are obtained, respectively, from F_D and F_L divided by $1/2\rho V^2 LD$, where ρ is the air density. Fig. 7 shows drag and lift coefficients as functions of the angle of attack, for the sectional model with and without lateral barriers, for a

Reynolds number ($Re = VD/\nu$) of about 100,000. As expected, the clearest effect of the barriers is a marked growth in the drag coefficient over the whole range of angles of attack. For positive angles, both barriers give rise to similar drag curves, while for negative angles the different porosity and distribution of the openings produce different trends of the coefficient. The peculiar drag coefficient pattern for the three deck layouts between 0° and 10° (exhibiting a bump between 5°) has been explained by flow visualizations through wool tufts attached to the sectional model (see Nicese, 2021). For the bare deck, the lift coefficient (Fig. 7(b)) exhibits a positive slope up to about $\alpha = 4°$, followed by a marked decreasing trend. The installation of Barrier 1 causes a decrease in the maximum lift value, and the peak is shifted towards lower values of α. With Barrier 2, the peak value of C_L is larger than for Barrier 1, and it is reached for an even lower angle of attack, very close to zero. Overall, the presence of the barriers makes more linear and steep the lift curve prior to the stall. In addition, the presence of the barriers extends the range of angles of attack for which the lift coefficient exhibits a negative slope. Therefore, according to the Den Hartog criterion (Den Hartog, 1956), lateral barriers (especially Barrier 2) increase the proneness of the bridge section to galloping instability for angles of attack of practical interest (say, between 0° and 4°), while a marked negative slope of the lift curve is experienced by the bare deck only for $\alpha \gtrsim 4°$ The expected galloping instability of this bridge section will further be discussed in Section 4.2.

Moreover, lift fluctuations are investigated in terms of Strouhal number (St) and dimensionless amplitude of the vortex-shedding force (C_{L0}), to make a first estimate of the proneness of the bridge section to vortex-induced vibration. The Strouhal number ($St = n_s D/V$) is determined from the frequency n_s associated with the dominant peak in the lift force spectrum. Fig. 8 shows the power spectral density of the lift coefficient at null, −3° and 3° angle of attack for the three cross-section layouts considered. These angles of attack are usually considered representative of a multitude of realistic cases, in the absence of extreme orographic features of the bridge site. The Strouhal frequency reduces in the presence of the lateral barriers (in particular, for Barrier 2) and both the broadness and the height of the spectral peak are remarkably affected by the presence and typology of the traffic barrier.

The coefficient C_{L0} is obtained as a sinusoidal equivalent amplitude based on the integration of the lift coefficient spectrum in a narrow frequency band fully embedding the Strouhal peak. An issue is the amplification of the measured fluctuating force close to the natural frequency of the static test setup. For this reason, C_{L0} is measured keeping the Strouhal frequency sufficiently below the resonance condition; moreover, the mechanical admittance function of the system is estimated to remove any possible amplification effects on C_{L0} (see Nicese, 2021, for further details). Table 2 reports the obtained values of the Strouhal number and C_{L0} coefficient for the three configurations and the three angles of attack. The same values are also graphically presented in Fig. 9, and they refer to a fairly low value of the Reynolds number (about 19,000), close to that at which aeroelastic tests are carried out. The presence of the barriers enhances vortex shedding. C_{L0} is particularly large for Barrier 1 at $\alpha = 0°$ and for Barrier 2 at $\alpha = -3°$ In contrast, vortex shedding for the configuration with Barrier 2 is only slightly stronger than for the bare deck when the angle of attack is $\alpha = 0°$

3.2. Aeroelastic tests

Aeroelastic tests are performed to determine the transverse VIV response of the bridge sectional model with and without lateral barriers at different angles of attack. The sectional model is let free to oscillate for increasing values of the wind velocity. In some cases, the measurements are also performed by decreasing the flow velocity to identify possible hysteresis effects in the lock-in range. Fig. 10 shows the response curves obtained for the lowest Scruton number tested, between about 3 and 4 (see also Table 3). For the bare deck, larger positive values of the flow angle of incidence are also tested, even if not reported in the present work (see Nicese, 2021). Results are plotted in terms of non-dimensional vibration amplitude y_{10}/D, where y_{10} is evaluated as the mean value of the 10 %-highest peaks in the transverse displacement time history, against reduced flow velocity $U = V/n_0 D$. Vortex-resonance reduced velocity based on static force measurements ($1/St$) is also indicated in the figure, along with the theoretical reduced velocity of motion-induced excitation/impinging shear-layer instability, calculated as $U^* = (B/D)/0.6$ (Nakamura and Nakashima, 1986; Naudascher and Wang,

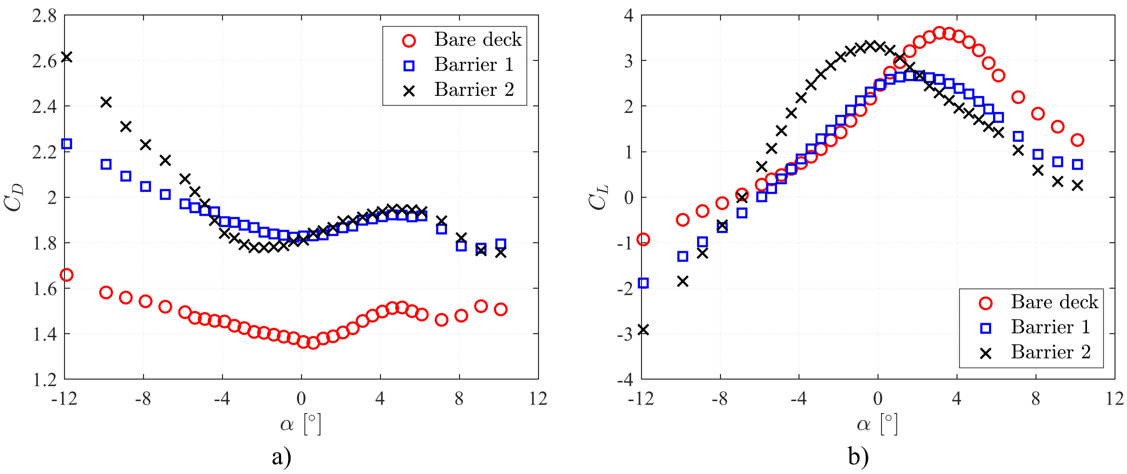

Fig. 7. Mean drag (a) and lift (b) coefficients for the sectional model with and without barriers (Re = 100,000).

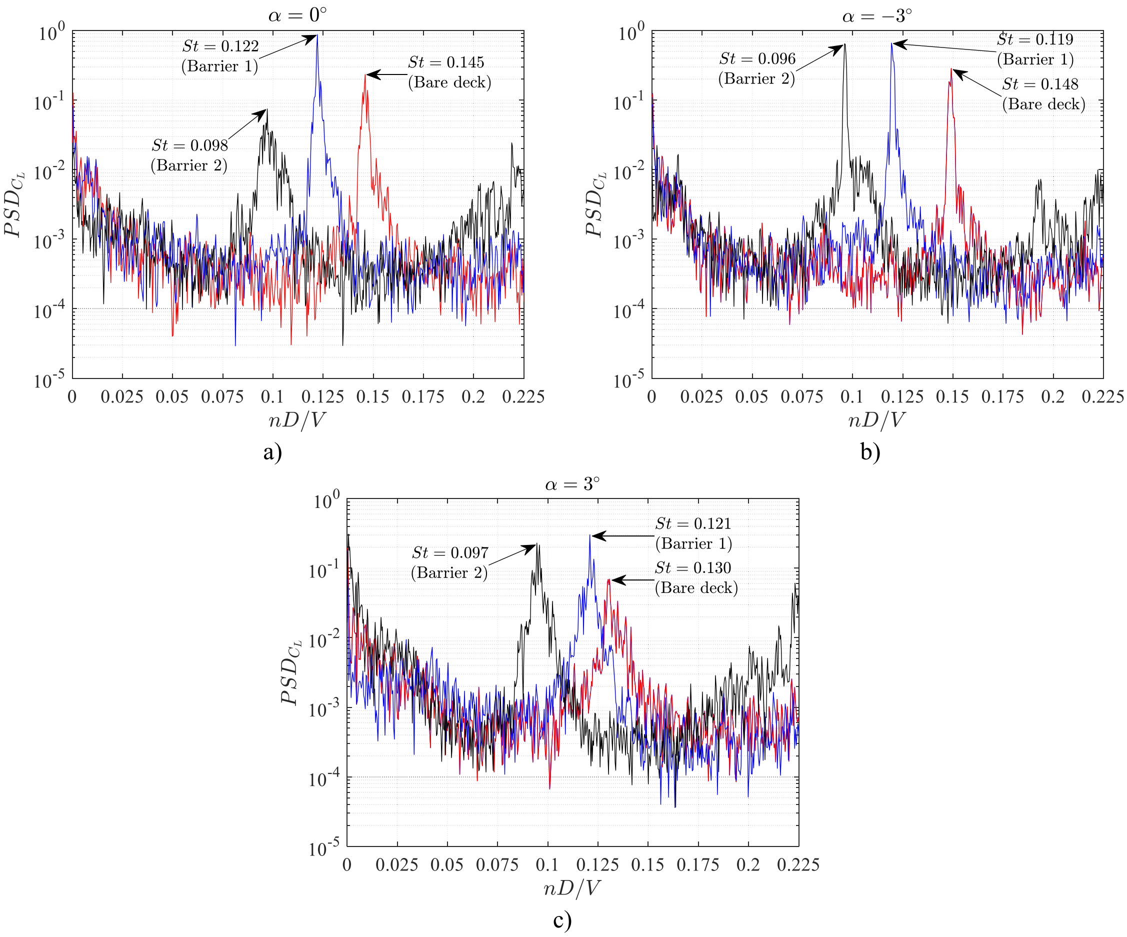

Fig. 8. Power spectral density of the lift coefficient at 0°, −3° and 3° flow angle of attack with and without lateral barriers (Re = 19,000). The spectral peaks corresponding to the Strouhal frequency are indicated.

Table 2
Strouhal number and amplitude of the vortex-shedding force for each configuration considered and for various angles of attack (Re = 19,000).

	α [°]	St [-]	C_{L0} [-]
Bare deck	0	0.145	0.24
	−3	0.148	0.23
	3	0.130	0.19
Barrier 1	0	0.122	0.38
	−3	0.119	0.36
	3	0.121	0.34
Barrier 2	0	0.098	0.28
	−3	0.096	0.36
	3	0.097	0.33

1993). In addition, secondary resonances and hysteresis effects, where relevant, are highlighted.

The bare deck gives rise to moderate vibration amplitudes and synchronization ranges for $-3^\circ \leq \alpha \leq 3^\circ$ (Fig. 10(a)). In particular, the lock-in curves at 0° and −3° are very similar to each other, with a narrow and nearly symmetric shape around the resonance velocity $1/St$. For $\alpha = 3^\circ$, the lock-in range slightly expands, and the peak response decreases from about 0.025D to 0.015D.

With the barriers, the variability in the VIV response markedly increases for the investigated angles of attack. In the case of Barrier 1 (Fig. 10(b)), the growth of the vibration amplitude is apparent. For a null angle of attack, the synchronization range slightly widens, while the oscillation amplitude increases up to 0.07D, which is almost three times the one experienced by the bare deck. For $\alpha = -3^\circ$, the maximum oscillation amplitude reaches a value of 0.05D, with a hysteresis loop at the lower bound of the lock-in range. For $\alpha = 3^\circ$,

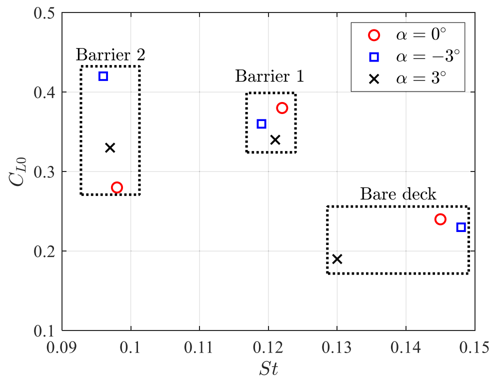

Fig. 9. Magnitude of the vortex-shedding lift coefficient against Strouhal number for the tested layouts at different angle of attack values (Re = 19,000).

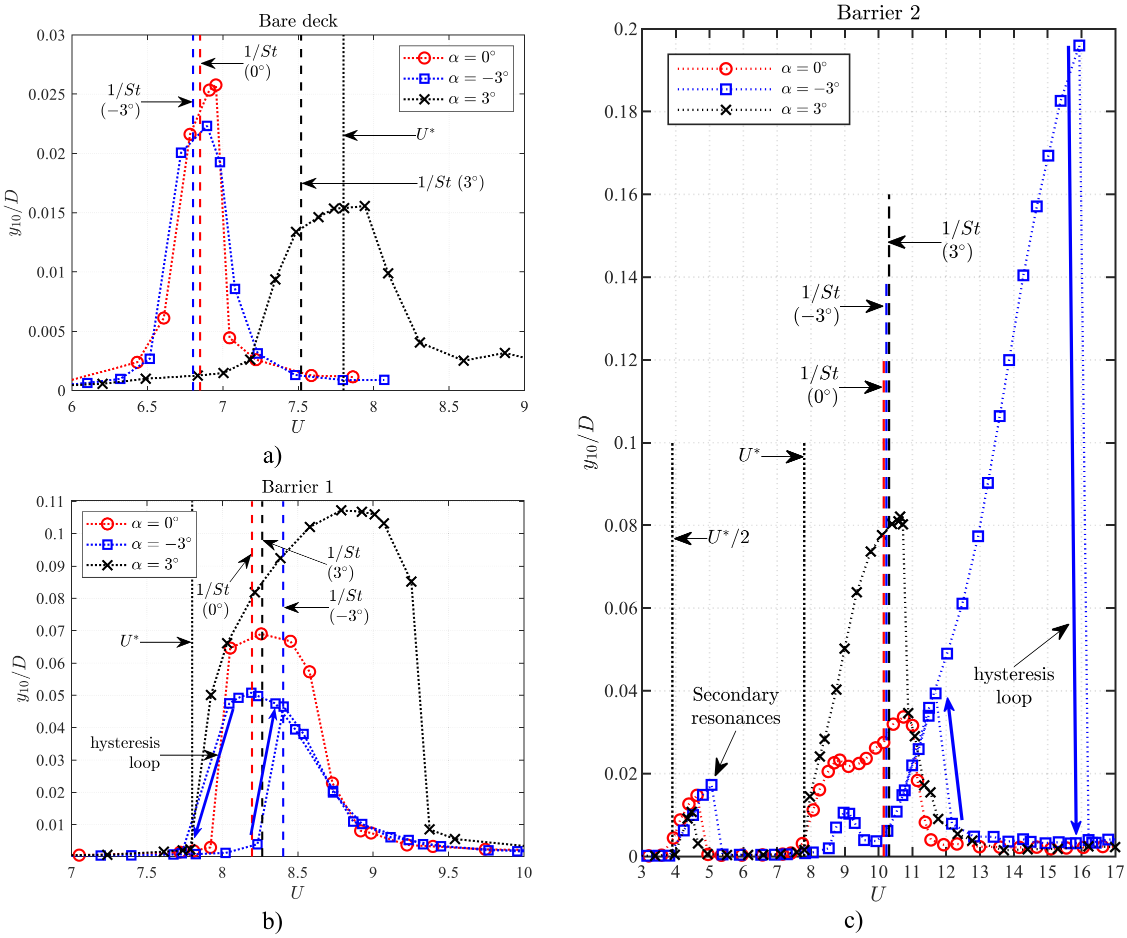

Fig. 10. Response curves at low Scruton number ($3 \leq Sc \leq 4$) for the bare deck (a), the deck equipped with Barrier 1 (b) and Barrier 2 (c) at different angles of attack ($0°$, $-3°$, $3°$). U and y_{10}/D denote the reduced wind velocity and the dimensionless transverse oscillation amplitude, respectively.

the lock-in range becomes much wider, and the peak amplitude exceeds $0.1D$. A certain increase in oscillation amplitude compared to the bare deck configuration was expected based on the measurements of the coefficient C_{L0} (Table 2); nevertheless, clearly, other aeroelastic effects must come into play to justify the abovementioned severe intensification of the response.

Barrier 2 produces wide lock-in ranges (Fig. 10(c)), but the peak vibration amplitudes are lower than for Barrier 1 for $\alpha = 0°$ and $\alpha = 3°$. In contrast, the results dramatically change for $\alpha = -3°$: a very large response is observed, with a wide hysteresis loop and an upper

Table 3
Scruton numbers related to the curves reported in Fig. 13 for each geometric layout and angle of attack.

	α [°]	Sc [-]			
		Sc_1	Sc_2	Sc_3	Sc_4
Bare deck	0	3.2	7.7	19.6	53.6
	−3	3.0	8.2	19.5	51.8
	3	3.3	7.5	17.5	50.6
Barrier 1	0	3.5	7.2	18.9	59.2
	−3	3.8	6.7	20.7	58.7
	3	3.4	12.2	29.5	62.2
Barrier 2	0	3.8	7.9	20.5	65.2
	−3	3.9	4.9	12.7	60.7
	3	3.5	12.5	28.2	59.9

branch reaching almost 0.2D. Nevertheless, such a high response is found only for low Scruton numbers, as the hysteresis loop and the upper branch already disappear for $Sc = 6.3$ (Fig. 11). Once again, static tests revealed that vortex shedding is strongest for $\alpha = -3^\circ$, but the measured value of C_{L0} (Table 2) does not justify such a large response increase. In addition, Barrier 2 promotes a peculiar shape of the lock-in curve for $\alpha = 0^\circ$ and $\alpha = -3^\circ$; indeed, a local peak in the response is evident before the growth to the maximum value. It is also worth noting that the lock-in onset for all the curves associated with Barrier 2 occurs for a reduced velocity which is significantly lower than $1/St$ (based on static tests) and close to U^*. Though less evident, this seems to occur for the cases with Barrier 1 too. Finally, with Barrier 2 a weaker secondary resonance response occurs around $U^*/2$, as is typical for the impinging shear-layer instability excitation mechanism at low Scruton number (Schewe, 1989; Marra et al., 2015).

Fig. 12 compares the VIV onset reduced velocity deduced from the abovementioned response curves of Fig. 10 with the data reported in Matsumoto (1999) for a collection of bridge girders and fundamental bluff bodies. For all the configurations studied in the current work, the onset of the VIV response might be consistent with the first mode of impinging shear-layer instability (or motion-induced excitation). The same may be said after a comparison with Fig. 2 in Naudascher and Wang (1993). However, this observation should not be overinterpreted as it is known that in some cases, especially for complex geometries, impinging shear-layer instability and Kármán-vortex excitation mechanisms can exhibit similar nondimensional frequencies and easily be confused from this point of view. It is also worth noting that the inclusion of the solid portion of the barriers in the normalizing cross-wind dimension (especially for Barrier 2) would slightly change the position of the markers in the figure but would not significantly alter the conclusions. We will further comment on this figure in Section 4.1.

Finally, Fig. 13 summarizes the results for all the bridge section layouts for $-3^\circ \le \alpha \le 3^\circ$ and various Scruton numbers (see Table 3). The impact of the Scruton number on vibration amplitude and lock-in range slightly changes from one layout to another; the sharpest impact of the Scruton number is observed for Barrier 2 at $\alpha = -3^\circ$, for which, as previously said, the oscillation amplitude does not decrease gradually with Sc but sharply drops for a nearly 30 %-change in the mass-damping parameter, namely from 4.9 to 6.3 (Fig. 11). In addition, except for this latter case, the lock-in curve pattern changes with the barrier type and with the flow angle of incidence, but it does not exhibit noticeable qualitative modifications due to the Scruton number.

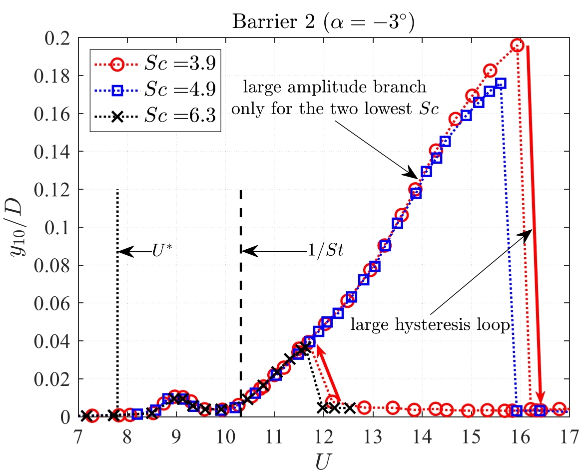

Fig. 11. Response curve for the deck equipped with Barrier 2 at $\alpha = -3^\circ$ for three different Scruton numbers. U and y_{10}/D denote the reduced wind velocity and the dimensionless transverse oscillation amplitude, respectively.

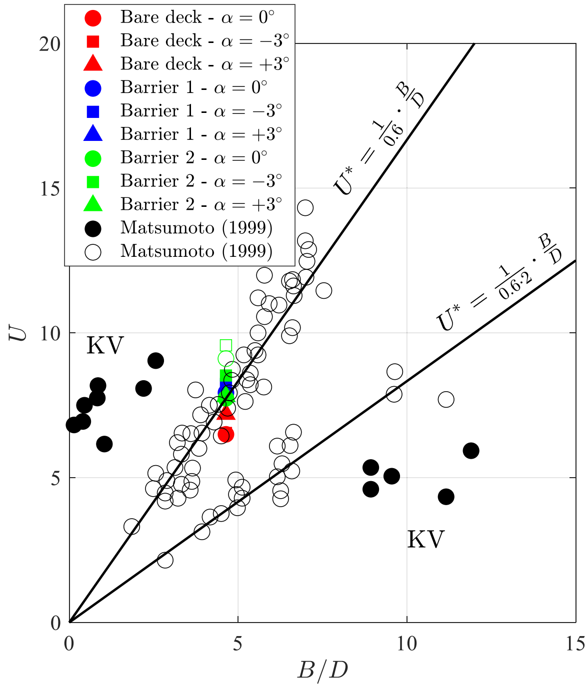

Fig. 12. Onset reduced velocity of VIV for the bridge deck configurations studied in the present work (determined from the response curves of Fig. 10) as a function of the section side ratio. Comparison with the data presented in Matsumoto (1999). Empty green markers for Barrier 2 refer to the reduced velocity at which the alleged Kármán-vortex excitation mechanism seems to become dominant in the VIV response curves. KV denotes the ranges where the Kármán-vortex excitation mechanism is responsible for VIV according to Matsumoto (1999), whereas the two straight lines indicate the theoretical onset velocity of motion-induced excitation (or impinging shear-layer instability).

3.3. *Wake-velocity measurements*

Flow-velocity measurements are carried out to examine in depth the vortex-shedding characteristics of the deck equipped with Barrier 2, which showed the most peculiar VIV features. Wind velocity fluctuations are measured through a hot-wire anemometer in the midspan plane perpendicular to the bridge model axis, while the latter is held fixed.

Fig. 14 shows the power spectral density of the velocity fluctuation for the probe located at position P1 (Fig. 6) for the angles of attack 0°, −3° and 3°, and different Reynolds numbers. The Strouhal peak, corresponding to the one detected through force measurements, is indicated in the figures, and no other narrow-band excitation at higher frequencies can be observed for $\alpha = 0°$ and $-3°$ at both low and high *Re*. In contrast, two different narrow-band contributions can be identified for $\alpha = 3°$. The first peak corresponds to the Strouhal frequency found with force measurements (named *St*), while the second, less energetic, peak occurs at a higher normalized frequency, named n^*. They are both visible for low Reynolds numbers (Fig. 14(e)), while they are less sharp for high Reynolds numbers (Fig. 14(f)). The nondimensional frequency n^* is equal to 0.124 if normalized with the bare deck depth D, but it becomes 0.58 if the deck width B is used for the normalization.

For $\alpha = 3°$, the tests are repeated with the probe in position P2, close to the leeward barrier (Fig. 6). Results are reported in Fig. 15. In this case, the Strouhal peak at *St* is visible neither at low nor at high *Re*, while that at n^* can still be observed. Therefore, coherent structures at the nondimensional frequency *St* do not occur in the flow field very close to the deck upper side, where only the mechanism related to n^* develops.

In conclusion, wake measurements suggest the coexistence of two vortex-excitation mechanisms for the deck equipped with Barrier 2 at an angle of attack of 3°. The peak detected at the nondimensional frequency n^* can reasonably be associated with impinging shear-layer instability since $n^* = 0.58$ (normalized with B) is close to the reference value of 0.6. On the other hand, the spectral peak related to the dimensionless frequency *St*, namely the frequency associated with the dominant peak in the lift force coefficient spectrum, might be associated with a Kármán-vortex excitation, probably promoted by the interaction behind the bridge deck of the shear layer separating from the lower side of the section and the vorticity overpassing the leeward traffic barrier. A schematic of these conjectured vortex-shedding mechanisms is reported in Fig. 16. Nevertheless, only detailed flow visualizations could confirm this assumption and offer insight into the actual features of these vortex-shedding mechanisms.

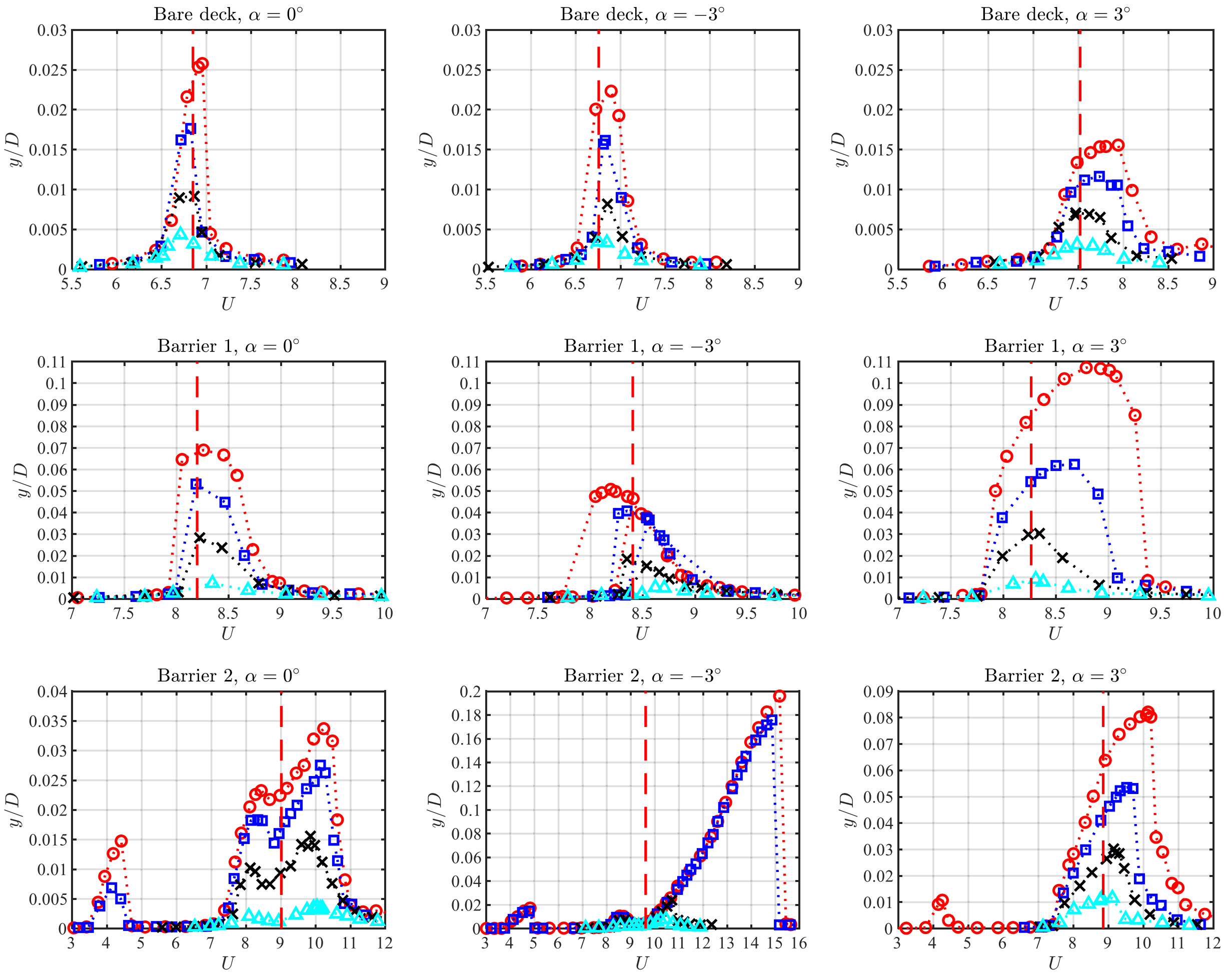

Fig. 13. Response curves for the bare deck and the deck equipped with lateral barriers for the angles of attack 0°, −3° and 3° and four Scruton number values tested (see Table 3 for the values and the markers). U and y_{10}/D denote the reduced wind velocity and the dimensionless transverse oscillation amplitude, respectively. The vortex-resonance reduced velocity based on static test results, $1/St$, is indicated by the red dashed line.

4. Discussion

4.1. Competing VIV excitation mechanisms

An increase in the susceptibility to VIV of a bridge section is usually expected to reduce the porosity of the barriers (see, e.g., Yan et al., 2022). In this study, the decrease in porosity from Barrier 1 to Barrier 2 also led to dramatic qualitative changes in the response patterns and several interesting features (Fig. 10(c)), such as a noticeable anticipation of the lock-in onset compared to the reduced velocity $1/St$ associated with the Strouhal number obtained with static force measurements. A noticeable peculiarity in the lock-in curve generated by Barrier 2 is shown in Fig. 17 for angles of attack of −3° and 0°. The trends highlighted by the arrows, exhibiting a secondary peak response in the first part of the synchronization range, suggest the possible coexistence of two excitation mechanisms. This is also supported by the data in Fig. 12, which shows that the onset of the response curve may be associated with an impinging shear-layer instability excitation, whereas the appearance of the second rising branch (empty green markers in Fig. 12) may be consistent with a Kármán vortex shedding resonance (interpreted as leading edge vortex shedding, LEVS, according to Naudascher and Wang (1993)). Nevertheless, the wake measurements for the stationary body discussed in Section 3.3 demonstrated the presence of two excitation mechanisms only for $\alpha = 3°$. Therefore, to examine this feature more in depth, wake measurements are repeated for the bridge model free to vibrate and inspected based on vibration results.

Fig. 18 shows the power spectral density of both flow-velocity fluctuations (PSD_v) measured in the wake of the model (position P1, see Fig. 6) and transverse vibrations (PSD_y), for a reduced velocity slightly lower than the lock-in onset. For $\alpha = 3°$, the coexistence of two contributions to transverse excitation observed for the stationary model (Fig. 14c) is confirmed in Fig. 18(a and b). The values of St and n^* are the same as for the stationary model case. The normalized natural frequency of the system (n_0*) is also indicated in the transverse vibration spectrum (Fig. 18b). In this case, the lock-in curve exhibits a monotonic increase up to the peak response, with the

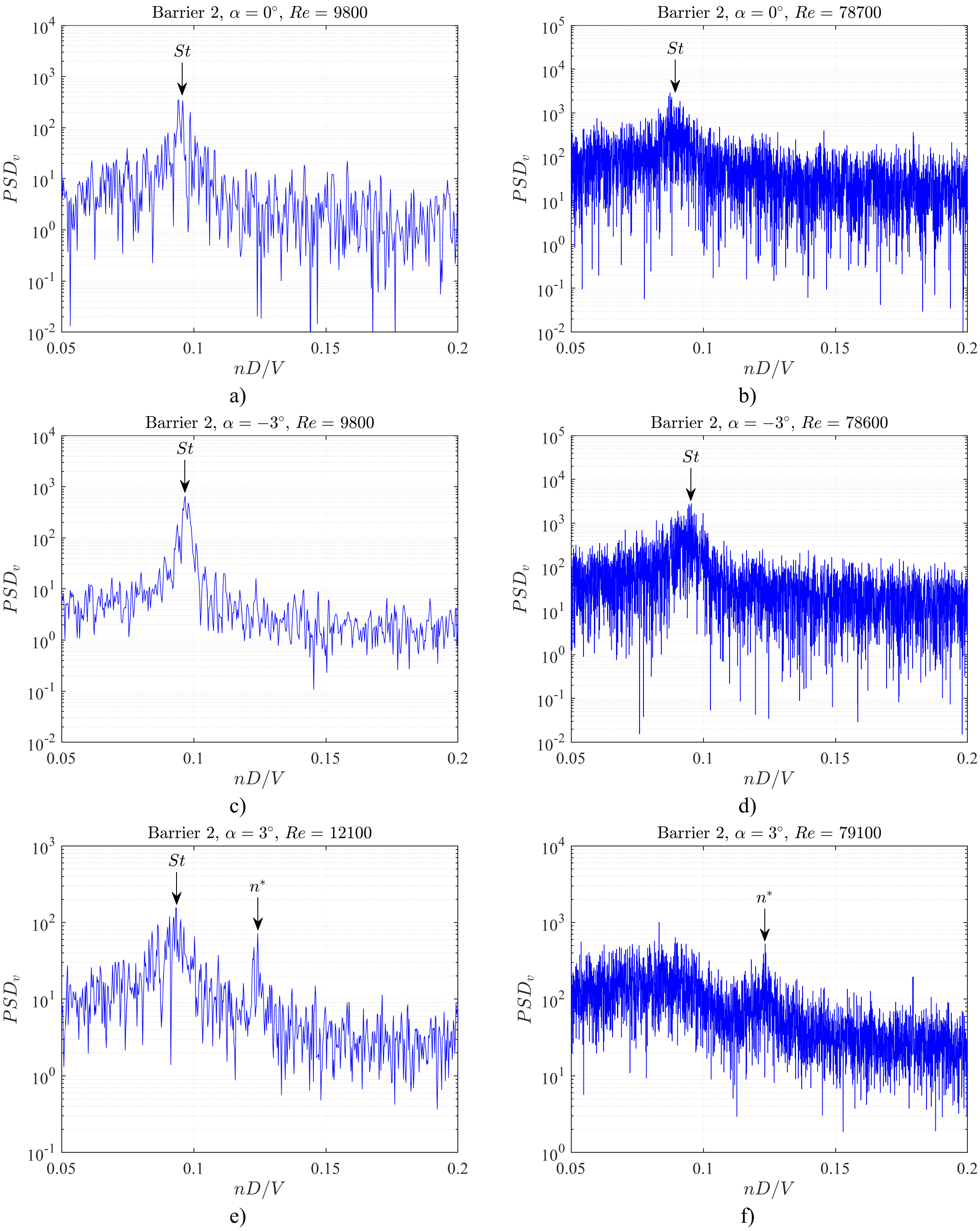

Fig. 14. Power spectral density of the flow-velocity measurements at position P1 (see Fig. 6) for the sectional model equipped with Barrier 2 and for an angle of attack of 0° (a, b), −3° (c, d) and 3° (e, f). Results refer to the model held stationary at two different Reynolds numbers.

abovementioned noticeable anticipation of the onset compared to the resonance velocity associated with the frequency *St* (Fig. 10c). The inspection of the response spectra corroborates the conjecture that this can be ascribed to the synchronization between the system vibration and the vortex-excitation at frequency n^*, when the alleged Kármán-vortex shedding frequency *St* is still quite far from the natural frequency; this is also the reason why in Fig. 18(b) the peak corresponding to n^* is much higher than that associated with *St*. Therefore, two vortex-excitation mechanisms seem to interact in the VIV response of the bridge.

For a null angle of incidence, flow-velocity measurements in the wake of the model before the lock-in onset (Fig. 18(c)) allow

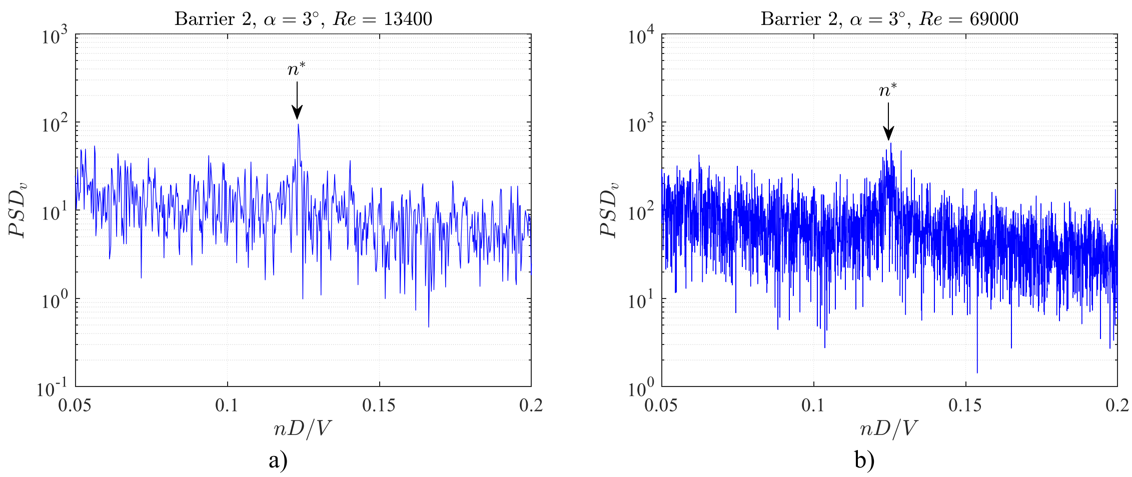

Fig. 15. Power spectral density of the flow-velocity measurements at position P2 (see Fig. 6) for the sectional model equipped with Barrier 2 and for an angle of attack of 3°. Results refer to the model held stationary at two different Reynolds numbers.

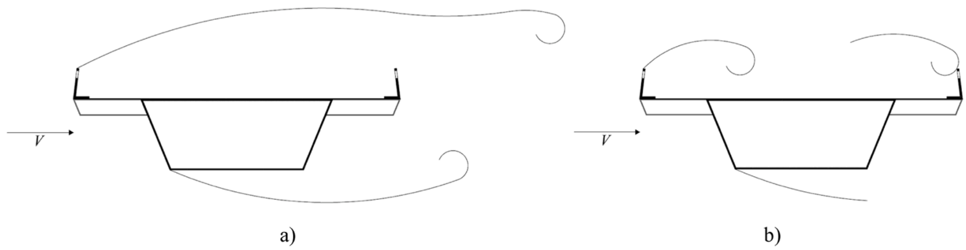

Fig. 16. Schematic of the conjectured mechanisms of vortex shedding: (a) Kármán vortex shedding (interpreted as leading edge vortex shedding, LEVS, according to Naudascher and Wang (1993)); (b) impinging shear-layer instability.

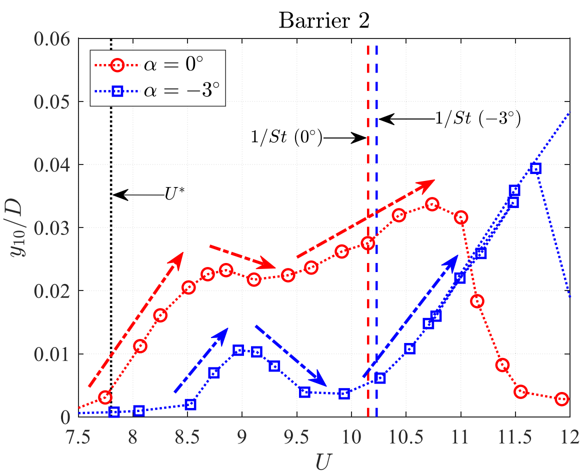

Fig. 17. Close up of the response curve between $U = 7.5$ and $U = 12$, where U denotes the reduced wind velocity, for the deck equipped with Barrier 2 and angles of attack of 0° and −3°.

identifying a dominant peak St and a minor contribution at $n^* = 0.122$ (which becomes 0.57 if normalized with B). Both peaks are also visible in the transverse displacement spectrum (Fig. 18d). In a similar way to what is stated for $\alpha = 3°$, the excitation at a higher frequency n^* causes the clear anticipation of the lock-in onset compared to the alleged Kármán-vortex resonance reduced velocity $1/St$ inferred from static force measurements. These results and the presence of two different excitation mechanisms comply with the two portions of the response curve highlighted in Fig. 17.

Finally, for the negative angle of attack $\alpha = -3°$, the wake flow velocity spectrum exhibits only a clear narrow-band peak at the

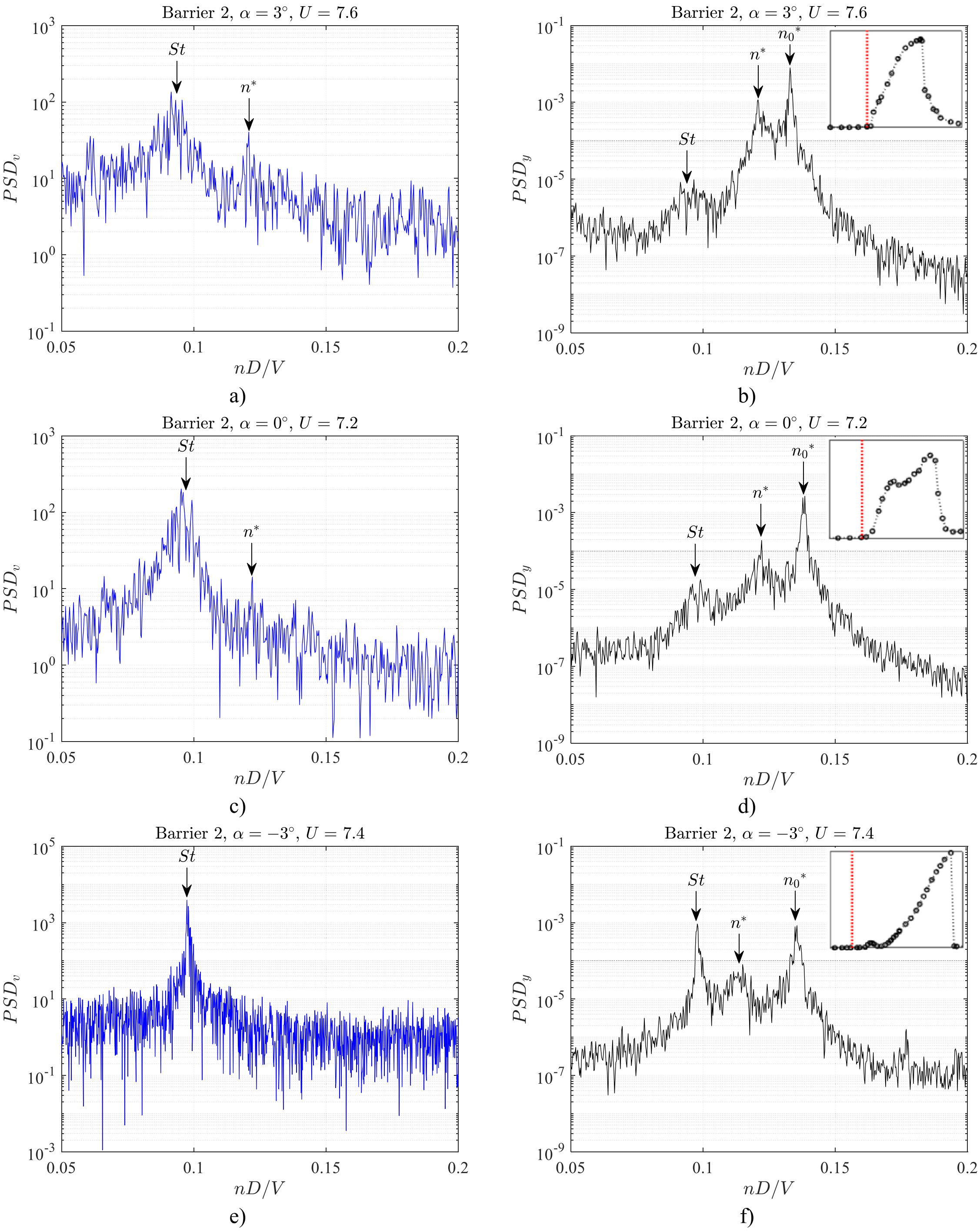

Fig. 18. Comparison between the power spectral density of the flow velocity at position P1 in the wake of the model equipped with Barrier 2 (a, c, e) and of the transverse vibration (b, d, f) for the considered angles of attack and a reduced velocity slightly lower than the lock-in onset (the Scruton number is between 3 and 4). The amplitude-velocity curves measured for the considered configurations are reported in the top-right box, where the dotted red line indicates the reduced velocity corresponding to the reported spectra.

frequency *St* (Fig. 18e), which is much more pronounced than in the previous two cases (as confirmed by the results reported in Table 2 and Fig. 14). Nevertheless, another small excitation contribution is visible in the displacement spectrum (Fig. 18f) at a reduced frequency of about 0.115 (0.53 if normalized with the deck width), indicated again as n^* in the figure. Fig. 19 shows that a weak synchronization regime occurs when n^* is very close to the natural frequency $n_0{}^*$, with the alleged Kármán-vortex shedding peak still far

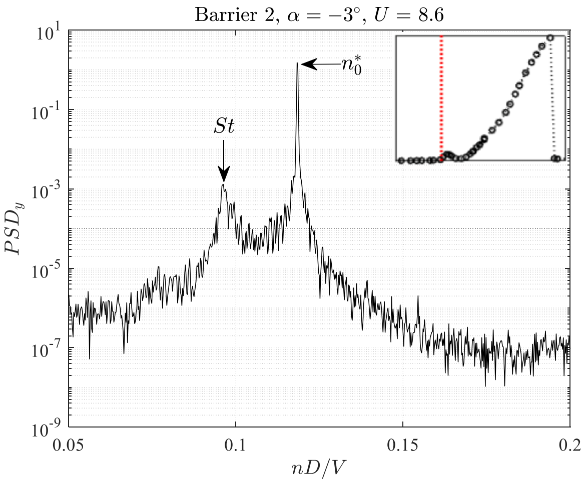

Fig. 19. Power spectral density of the transverse displacement of the model equipped with Barrier 2 at $\alpha = -3°$ for a reduced velocity slightly higher than the onset of the first weak synchronization range, as indicated in the top-right box.

from the resonance condition. This confirms that the small first part of the lock-in curve, over a reduced velocity range between 8.5 and 9.5 (Fig. 10(c), Fig. 11 and Fig. 17), may not be promoted by the Kármán-vortex shedding mechanism observed during static force measurements, but by a secondary excitation mechanism.

Therefore, when the model is free to vibrate, two vortex-shedding excitation mechanisms seem to interact for all the three angles of attack considered, and not just for $\alpha = 3°$ as one may have inferred from the results of static tests. As mentioned in Section 3.3, the secondary n^*-peaks might be ascribable to impinging shear-layer instability, since its values are compatible with those reported for instance by Nakamura and Nakashima (1986), Naudascher and Wang (1993) and Matsumoto (1999) for this phenomenon. This seems reasonable if one considers how the second typology of barriers modifies the bridge section geometry, with the solid lower portion of the barrier that promotes a sort of H-shape of the cross section. While for $\alpha = 3°$ the intensity of the alleged impinging shear-layer instability is sufficiently strong to be observed even in stationary conditions, for $\alpha = 0°$ and $\alpha = -3°$ a slight vibration of the body is necessary to trigger this secondary excitation mechanism. In this regard, it is worth noting that Naudascher and Wang (1993) identified two different behaviors for stationary rectangular prisms: for a side ratio between 2 and 8, the vortex formation is controlled by a mechanism equivalent to the impinging-shear layer instability of flow past cavities (Rockwell and Naudascher, 1978), while between 8 and 16 the same phenomenon is usually too weak to be identified without an external trigger, such as a sound field (Stokes and Welsh, 1986) or a slight motion of the leading edge of the body. Interestingly, in the present case study the ratio between the deck width and the solid lower portion of the barrier is about 15.5.

According to Shiraishi and Matsumoto (1983), when Kármán-vortex excitation and impinging shear-layer instability coexist, the onset of the lock-in curve is no longer strictly correlated with the resonance reduced velocity $1/St$. By introducing a certain level of turbulence in the incoming flow or a splitter plate in the wake of a 4:1 rectangular cylinder and a hexagonal bridge section, Matsumoto et al. (1993) demonstrated that the two mechanisms mutually disturb. Indeed, in this way the Kármán-vortex shedding is reduced or suppressed, and the wind-induced vibration, driven only by the impinging shear-layer instability, becomes larger. Based on this concept of competing mechanisms, it seems reasonable in the present case that the largest oscillation amplitude occurs for $\alpha = -3°$, when the Kármán-vortex shedding mechanism is probably strongest and the impinging shear-layer instability mechanism weakest (Fig. 14(c) and Fig. 18(e and f)), and the interference between them is very limited. However, in this case, the dramatic drop in the response for the abovementioned increment of about 30 % in the Scruton number (Fig. 11) remains unexplained. In addition, the presence of competing vortex-excitation mechanisms alone is not able to explain why the oscillation amplitudes are higher for $\alpha = 3°$ than for $\alpha = 0°$ since the strongest contribution from impinging shear-layer instability is observed in the former case (Fig. 18a) but the peak oscillation amplitude is also slightly larger. Nevertheless, this is not too surprising, considering the remarkably different aerodynamics for the two angles of attack when Barrier 2 is installed (Fig. 7) and the higher intensity of the alleged Kármán-vortex shedding revealed by static force measurements for $\alpha = 3°$ (see C_{L0} values in Table 2).

Finally, the identification of two clear portions in the response curve, as in the current work for $\alpha = 0°$ and $\alpha = -3°$, to the Authors' best knowledge, has been documented only in very few cases in the literature. An example is provided by Matsumoto et al. (1993) and Matsumoto (1999) for the torsional response of a 4:1 rectangular cylinder with the rotation axis fixed behind the trailing edge: two local peak responses are identified at reduced velocities corresponding to motion-induced and Kármán-vortex excitations, while only the peak associated with the former mechanism is detected after installing a splitter plate, which also significantly enhances the maximum response amplitude. Another example is represented by the low-speed small response found by Mannini et al. (2016) for a 3:2 rectangular cylinder at low Scruton number and ascribed to a weak resonance with a secondary mechanism of impinging shear-layer instability.

4.2. Predictions of galloping instability

As noted in Section 3.1, the aerodynamic force coefficients for different angles of attack point out that, according to the quasi-steady theory, some of the test cases considered are expected to exhibit galloping instability in the velocity range explored during aeroelastic tests. In this regard, the transverse force coefficient C_{Fy} is reported in Fig. 20, evaluated based on static force measurements in the following way:

$$C_{Fy}(\alpha) = -\sec(\alpha)[C_L(\alpha) + C_D(\alpha)\tan(\alpha)] \tag{1}$$

As expected, the effect of the lateral barriers on C_{Fy} is noticeable. In particular, for Barrier 2 and $\alpha = 3^\circ$ the slope of the transverse force coefficient C_{Fy} is largely positive, suggesting a marked proneness to galloping instability according to the Den Hartog criterion (Den Hartog, 1956). Transverse instability is here predicted, for the lowest mechanical damping tested, at a reduced velocity of about $U = 2$, which is much lower than the vortex-resonance reduced velocity $1/St$. In this case, quenching of the galloping instability may be expected up to the vortex-resonance velocity, followed by the onset of a divergent instability (Parkinson and Wawzonek, 1981; Mannini et al., 2014, 2018). In contrast, such instability is not observed during the aeroelastic tests (not even beyond the wind speed range shown in Fig. 9(c)). Another example of mismatch with the quasi-steady theory is encountered for the bare deck at $\alpha = 8.5^\circ$ (see Nicese, 2021), even if these results are not included here for the sake of brevity.

For a deeper investigation of this issue, experimental measurements of the aerodynamic damping (ζ_{aero}) are carried out by means of specific free-decay tests. The model installed on the aeroelastic setup (Fig. 4(b)) is released from an initial condition of transverse displacement, and the following oscillation time history is recorded. The aerodynamic damping is determined by the difference between the total damping measured under wind and the mechanical damping in still air. The tests are performed outside the lock-in range, both at low and high reduced velocities, since in the latter case the quasi-steady theory is expected to be more accurate. The measured aerodynamic damping is then compared to the values predicted by the quasi-steady theory, evaluated as follows:

$$\zeta_{aero}^{QS} = -\frac{\rho D^2 L}{8\pi M} \cdot \frac{dC_{Fy}}{d\alpha} \cdot U \tag{2}$$

Fig. 21 reports a selection of representative results, including the abovementioned case of the deck equipped with Barrier 2 at $\alpha = 3^\circ$ The experimental values are almost everywhere positive, in clear contrast to the negative quasi-steady predictions (Fig. 21f) in spite of the high reduced velocity reached in the experiments (nearly 65). A similar result is obtained for the deck equipped with Barrier 2 at a null angle of attack (Fig. 21d) and with Barrier 1 at $\alpha = 3^\circ$ (Fig. 21e), although in these cases the negative trend of the quasi-steady aerodynamic damping is less pronounced, and instability is not predicted within the reduced velocity range tested in the wind tunnel. In contrast, Fig. 21(a– c) reports three configurations (bare deck and deck equipped with barriers, for an angle of attack of -3°), for which the measurements exhibit a much better agreement with the quasi-steady theory. In particular, the best predictions are obtained for the bare deck and the deck equipped with Barrier 1 (Fig. 21(a and c)), for which $\alpha = -3^\circ$ is much lower than the angle of attack associated with stall. In contrast, the accuracy of the quasi-steady results seems to slightly degrade with Barrier 2 (Fig. 21b), when the C_{Fy} curve changes its slope from negative to positive close to $\alpha = -3^\circ$ Surprisingly, in these three cases, reasonable predictions are found even at low reduced velocity, where the quasi-steady theory is not supposed to be applicable.

The qualitative discrepancy between the quasi-steady theory and the experimental evidence has already been observed in the literature for other geometries, such as for a square cylinder at an angle of attack of 12° (Carassale et al., 2015), and for a bridge trapezoidal open section at $\alpha = -4^\circ$ (Chen et al., 2020), but a clear explanation for that has not been provided yet. Such an issue will deserve due attention in the future, as it represents a serious problem in engineering practice for galloping predictions. However, the understanding of the physical reasons for the failure of the quasi-steady theory is also important from a VIV response modeling perspective, since the quasi-steady theory is also employed in some VIV mathematical models to account for the aerodynamic damping contribution not associated with the vortex shedding (e.g., Tamura and Shimada, 1987; Corless and Parkinson, 1988; Marra et al., 2017; Mannini et al., 2018).

4.3. Comparison with the Volgograd Bridge response

A comparison between the experimental response of the sectional model considered in the present work and that of the Volgograd Bridge, by which it is inspired, may be of interest. The information about the incoming flow during the famous VIV event in 2010 is limited and mostly provided by Corriols and Morgenthal (2012), Weber et al. (2013), and Corriols (2015). The Volgograd Bridge exhibited violent vibrations for a wind velocity between 11.6 m s^{-1} and 15.6 m s^{-1}, which, for a first bending frequency of 0.45 Hz and a cross-flow size of the bare deck of 3.61 m, leads to an estimate of the Strouhal number between 0.104 and 0.140. The value of St for the sectional model equipped with Barrier 1 (fairly similar to that installed on the real bridge), is about 0.12 for an angle of attack ranging from -3° to 3° (Table 2). The maximum vibration amplitude exhibited by the bridge in May 2010 was about 40 cm, corresponding to 0.11 in dimensionless form (being normalized with the bare deck depth). Fig. 22 reports the maximum vibration amplitude against the Scruton number for the wind tunnel model, while the triangular marker refers to the Volgograd Bridge prototype; for the latter, the estimate of the Scruton number is based on the data available in the literature and an assumed value of the structural damping of 0.003 according to EN 1991–1–4 (2010), since no information is available about this parameter. The peak response of the Volgograd Bridge lays between the results obtained in the wind tunnel for $\alpha = 0^\circ$ and $\alpha = 3^\circ$.

However, as mentioned in Section 2.1, the wind tunnel model has a symmetric cross-section, while the prototype bridge presents a

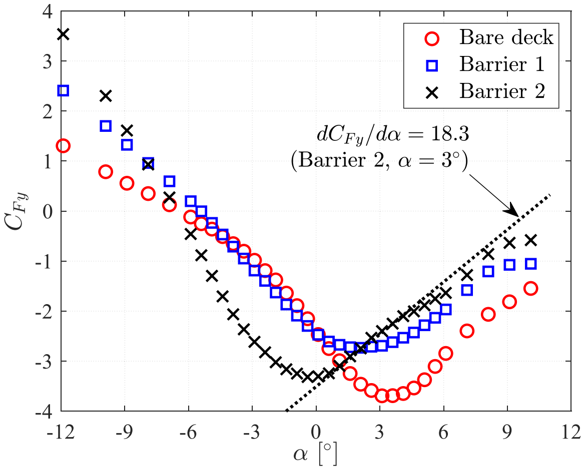

Fig. 20. Quasi-steady transverse force coefficient at different angles of attack for the sectional model with and without barriers (Re = 100,000). The positive slope related to Barrier 2 at $\alpha = 3°$ is indicated.

pedestrian walkway only on one side. Moreover, the latter is inclined of about 1° Therefore, assuming a horizontal incoming flow, the relative angle of attack would be equal to −1° In addition, during the violent VIV event in 2010, the Volgograd Bridge was exposed to a skew wind with respect to the bridge axis. All these uncertainties, along with those affecting the Scruton number of the prototype, must be considered in the comparison reported in Fig. 22. Despite this, the current wind tunnel campaign provides results that reasonably comply with the full-scale observations.

5. Conclusions

The present work deals with the VIV response of a non-streamlined box section, typically adopted for girder bridges, equipped with realistic traffic barriers and presenting a high ratio of barrier height to deck width and depth. The collection of literature works reported in Table 1 not only highlights the limited number of studies for this bridge typology but also provides an extended and detailed database, which may be useful for future research dealing with bridge VIV response and the effects of screens or barriers.

The current experimental study showed that the typology of barriers, along with small variations in the angle of attack, can dramatically change the VIV response, not only in terms of peak vibration amplitude but also in terms of lock-in response pattern. Partially solid traffic barriers or low-porosity pedestrian parapets (for instance, those realized in glass-like materials for aesthetic purposes) may even completely overturn the behavior of a non-streamlined section geometry, giving rise to a violent VIV response, incompatible with the bridge usage. This is particularly meaningful given the uncommon aerodynamic optimization of barriers other than for long-span cable-stayed and suspension bridges.

Low-porosity barriers, especially in the presence of a continuous solid portion in contact with the deck surface (generating a cavity on the deck upper side), can alter the vortex shedding characteristics and may promote or strengthen impinging shear-layer instability. The possible interaction between this excitation mechanism and the Kármán-vortex shedding may not be detected through static tests, commonly employed to determine the Strouhal number of a bridge section. From the engineering practice point of view, this may result in a significant anticipation of the lock-in onset compared to the predictions based on the Strouhal number and lead to a significant VIV response below the design wind speed.

Kármán-vortex shedding and impinging shear-layer instability seem to interfere and disturb each other; indeed, the largest VIV response with the less-porous barrier is observed for the angle of attack for which the second mechanism is weakest. In some cases, multiple excitation mechanisms are even inferable from the lock-in curve morphology. Although the conjecture of interacting vortex-shedding mechanisms is supported by the experimental evidence (in particular by the wake-velocity measurements discussed in Section 3.3 and Section 4.1), a solid proof of it requires high-quality flow visualizations. Additional wind tunnel tests with a splitter plate behind the bridge sectional model may also be very useful. These tasks must be carried out in the future, either by the Authors of the present work or by other research groups. Another possible development of the present work might be the modeling of VIV bridge response through a double wake-oscillator model like the one recently proposed by Hui et al. (2024) and successfully applied to the case of a 4:1 rectangular cylinder. Nevertheless, some modifications of the model might be necessary to capture correctly the abovementioned interfering excitation mechanisms.

Finally, the current results highlight the failure of the quasi-steady theory in predicting transverse divergent instabilities for some of the considered test cases (in particular, close or beyond the angle of the stall, while where a good prediction is obtained at high reduced velocity it is found at low reduced velocity too, where the quasi-steady theory is not supposed to be applicable), as confirmed by the direct measurement of the aerodynamic damping at high reduced wind speed. Such a behavior, already encountered in the literature for other bluff cross sections, has not been explained yet and represents an important open issue.

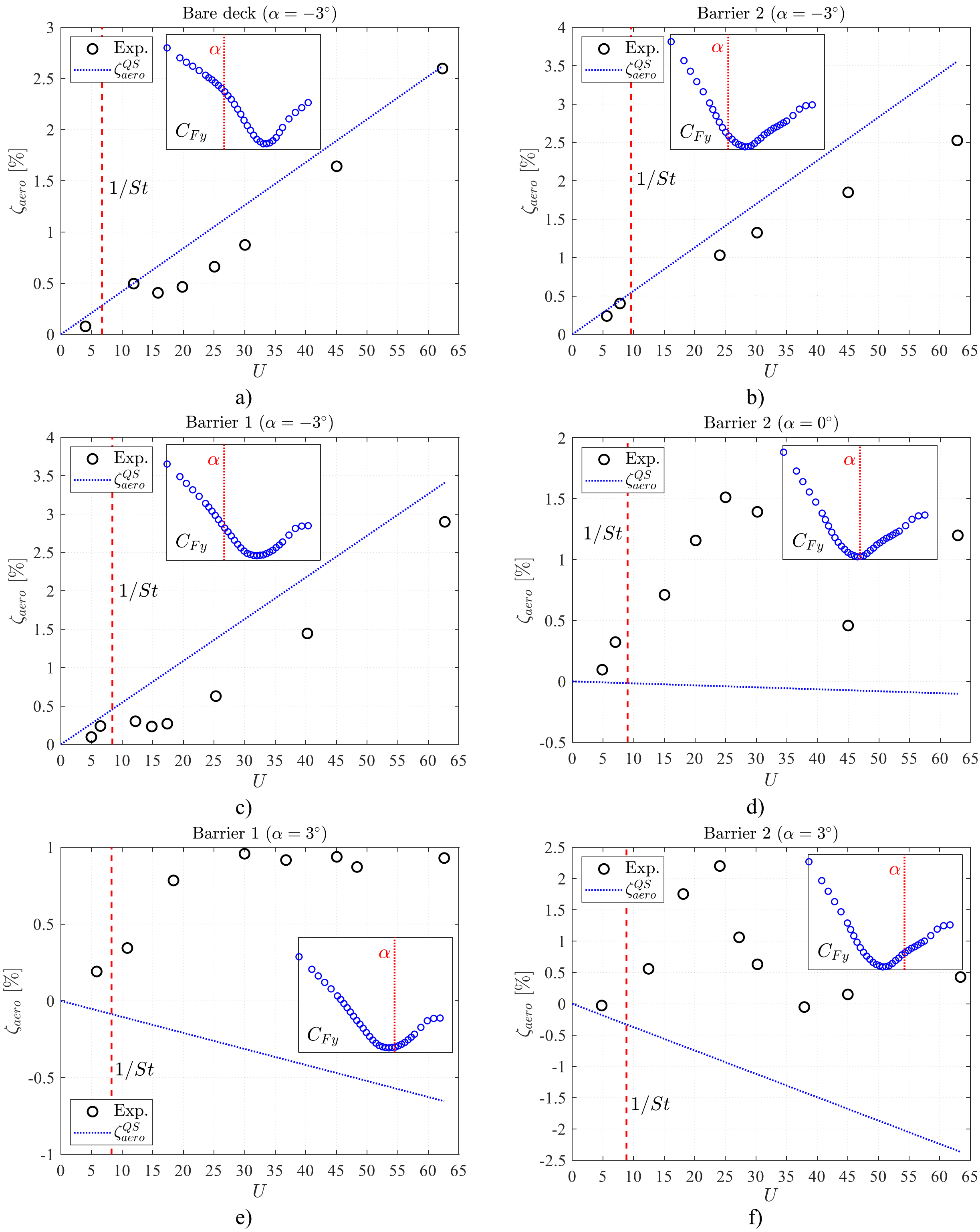

Fig. 21. Aerodynamic damping measured via free-decay tests for various bridge deck configurations and angles of attack, for different values of the reduced wind velocity U. The dotted vertical line in the subplots identifies the point in the transverse force coefficient pattern related to the tested angle of attack.

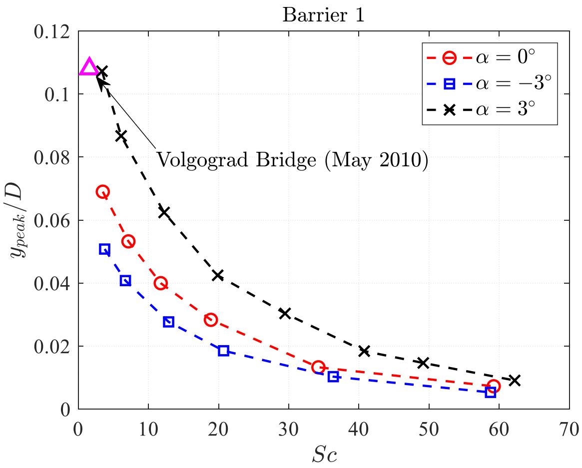

Fig. 22. Dimensionless peak vibration amplitude against Scruton number for the sectional model equipped with Barrier 1 and comparison with the estimate for the VIV event occurring in May 2010 for the Volgograd Bridge.

CRediT authorship contribution statement

Bernardo Nicese: Writing – review & editing, Writing – original draft, Investigation, Formal analysis, Visualization, Methodology. **Antonino Maria Marra:** Writing – review & editing, Supervision, Methodology, Conceptualization. **Gianni Bartoli:** Supervision. **Claudio Mannini:** Writing – review & editing, Supervision, Methodology, Conceptualization.

Declaration of competing interest

The authors declare that they have no known competing financial interests or personal relationships that could have appeared to influence the work reported in this paper.

Data availability

Data will be made available on request.

References

Bai, H., Ji, N., Xu, G., Li, J., 2020. An alternative aerodynamic mitigation measure for improving bridge flutter and vortex induced vibration (VIV) stability: sealed traffic barrier. J. Wind Eng. Ind. Aerodyn. 206, 104302.

Bartoli, G., Contri, S., Mannini, C., Righi, M., 2009. Toward an improvement in the identification of bridge deck flutter derivatives. J. Eng. Mech. 135 (8), 771–785.

Battista, R.C., Pfeil, M.S., 2000. Reduction of vortex-induced oscillations of Rio-Niterói bridge by dynamic control devices. J. Wind Eng. Ind. Aerodyn. 84, 273–288.

Carassale, L.F., 2015. Motion-excited forces acting on a square prism: a qualitative analysis. In: Proceedings of 14th International Conference on Wind Engineering. Porto Alegre, Brazil.

Chen, C., Mannini, C., Bartoli, G., Thiele, K., 2020. Experimental study and mathematical modeling on the unsteady galloping of a bridge deck with open cross section. J. Wind Eng. Ind. Aerodyn. 203, 104170.

Chen, Z., Liu, S., Yu, X., Ma, C., Liu, L., 2017. Experimental Investigations on VIV of bridge deck sections: a case study. KSCE J. Civ. Eng. 21, 2821–2827.

Corless, R.M., Parkinson, G.V., 1988. A model of the combined effects of vortex-induced oscillation and galloping. J. Fluids Struct. 2, 203–220.

Corriols, A.S., 2015. Vortex-induced vibrations on bridges. The interaction mechanism in complex sections and a new proposed semi-empirical model. Technical University of Madrid, Madrid, Spain. Ph.D. Thesis.

Corriols, A.S., Morgenthal, G., 2012. Computational analysis of VIV observed on existing bridges. In: Proceedings of The Seventh International Colloquium on Bluff Body Aerodynamics and Applications (BBAA7). Shanghai, China.

Hartog, Den, P, J., 1956. Mechanical Vibrations, 4th ed. McGraw-Hill, New York. Reprinted by Dover, New York, 1984.

Ehsan, F., Scanlan, R.H., 1990. Vortex-induced vibrations of flexible bridges. J. Eng. Mech. 116 (6), 1392–1411.

Frandsen, J.B., 2001. Simultaneous pressures and accelerations measured full-scale on the Great Belt East suspension bridge. J. Wind Eng. Ind. Aerodyn. 89, 95–129.

Fujino, Y., Yoshida, Y., 2002. Wind-induced vibration and control of Trans-Tokyo Bay Crossing Bridge. J. Struct. Eng. 128, 1012–1025.

Ge, Y., Zhao, L., Cao, J., 2022. Case study of vortex-induced vibration and mitigation mechanism for a long-span suspension bridge. J. Wind Eng. Ind. Aerodyn. 220, 104866.

Honda, A., Ito, M., Kimura, H., 1992. Aerodynamic instability of prestressed concrete cable-stayed bridge with noise barrier. J. Wind Eng. Ind. Aerodyn. 41-44, 1169–1180.

Hu, C., Zhao, L., Ge, Y., 2018. Time-frequency evolutionary characteristics of aerodynamic forces around a streamlined closed-box girder during vortex-induced vibration. J. Wind Eng. Ind. Aerodyn. 182, 330–343.

Hui, Y., Tang, Y., Yang, Q., Chen, B., 2024. A wake-oscillator model for predicting VIV of a 4-to-1 rectangular cylinder. Nonlinear Dyn. 112, 8985–8999.

Hwang, Y.C., Kim, S., Kim, H.K., 2019. Cause investigation of high-mode vortex-induced vibration in a long-span suspension bridge. Struct. Infrastruct. Eng. 16, 84–93.

Kubo, Y., Kimura, K., Sadashima, K., Okamoto, Y., Yamaguchi, E., Kato, K., 2002. Aerodynamic performance of improved shallow π shape bridge deck. J. Wind Eng. Ind. Aerodyn. 90, 2113–2125.

Kumarasena, T., Scanlan, R.H., Ehsan, F., 1991. Wind-induced motions of the Deer Isle Bridge. J. Struct. Eng. 117, 3356–3374.

Larose, G.L., Larsen, S.V., Larsen, A., Hui, M., Jensen, A.G., 2003. Sectional model experiments at high Reynolds number for the deck of a 1018 m span cable-stayed bridge. In: Proceedings of 11th International Conference on Wind Engineering. Lubbock, TX, USA, pp. 373–380.
Larsen, A., 1993. Aerodynamic aspects of the final design of the 1624 m suspension bridge across the Great Belt. J. Wind Eng. Ind. Aerodyn. 48, 261–285.
Larsen, A., Wall, A., 2012. Shaping of bridge box girders to avoid vortex shedding response. J. Wind Eng. Ind. Aerodyn. 104-106, 159–165.
Larsen, A., Esdahl, S., Andersen, J.E., Vejrum, T., 2000. Storebælt suspension bridge - vortex shedding excitation and mitigation by guide vanes. J. Wind Eng. Ind. Aerodyn. 88, 283–296.
Larsen, A., Savage, M., Lafrenière, A., Hui, M.C., Larsen, S.V., 2008. Investigation of vortex response of a twin box bridge section at high and low Reynolds numbers. J. Wind Eng. Ind. Aerodyn. 96, 934–944.
Larsen, A., Svensson, E., Andersen, H., 1995. Design aspects of tuned mass dampers for the Great Belt East Bridge approach spans. J. Wind Eng. Ind. Aerodyn. 54/55, 413–426.
Li, M., Sun, Y., Jing, H., Li, M., 2018. Vortex-induced vibration optimization of a wide streamline box girder by wind tunnel test. KSCE J. Civ. Eng. 22 (12), 5145–5153.
Macdonald, J.H., Irwin, P.A., Fletcher, M.S, 2002. Vortex-induced vibrations of the Second Severn Crossing cable-stayed bridge - full-scale and wind tunnel measurements. Proceedings of the Institution of Civil Engineers - Structures and Buildings 152, 123–134.
Mannini, C., Marra, A.M., Bartoli, G., 2014. VIV–galloping instability of rectangular cylinders: review and new experiments. J. Wind Eng. Ind. Aerodyn. 132, 109–124.
Mannini, C., Marra, A.M., Massai, T., Bartoli, G., 2016. Interference of vortex-induced vibration and transverse galloping for a rectangular cylinder. J. Fluids Struct. 66, 403–423.
Mannini, C., Marra, A.M., Pigolotti, L., Bartoli, G., 2017. The effects of free-stream turbulence and angle of attack on the aerodynamics of a cylinder with rectangular 5:1 cross section. J. Wind Eng. Ind. Aerodyn. 161, 42–58.
Mannini, C., Massai, T., Marra, A.M., 2018a. Modeling the interference of vortex-induced vibration and galloping for a slender rectangular prism. J. Sound Vib. 419, 493–509.
Mannini, C., Massai, T., Marra, A.M., 2018b. Unsteady galloping of a rectangular cylinder in turbulent flow. J. Wind Eng. Ind. Aerodyn. 173, 210–226.
Marra, A.M., Mannini, C., Bartoli, G., 2011. Van der Pol-type equation for modeling vortex-induced oscillations of bridge decks. J. Wind Eng. Ind. Aerodyn. 99 (6–7), 776–785.
Marra, A.M., Mannini, C., Bartoli, G., 2015. Measurements and improved model of vortex-induced vibration for an elongated rectangular cylinder. J. Wind Eng. Ind. Aerodyn. 145, 358–367.
Marra, A.M., Mannini, C., Bartoli, G., 2017. Modeling of vortex-induced vibrations of an elongated rectangular cylinder through wake-oscillator models. In: Proceedings of the 7th European and African Conference on Wind Engineering. Liège, Belgium.
Matsumoto, M., 1999. Vortex shedding of bluff bodies: a review. J. Fluids Struct. 13, 791–811.
Matsumoto, M., Shiraishi, N., Shirato, H., Stoyanoff, S., Yagi, T., 1993. Mechanism of, and turbulence effect on vortex-induced oscillations for bridge box girders. J. Wind Eng. Ind. Aerodyn. 49, 467–476.
Matsumoto, M., Shirato, H., Yagi, T., Shijo, R., Eguchi, A., Tamaki, H., 2003. Effects of aerodynamic interferences between heaving and torsional vibration of bridge decks: the case of Tacoma Narrows Bridge. J. Wind Eng. Ind. Aerodyn. 91 (12-15), 1547–1557.
Meng, X., Zhu, L., Guo, Z., 2011. Aerodynamic interference effects and mitigation measures on vortex-induced vibrations of two adjacent cable-stayed bridges. Frontiers of Architecture and Civil Eng. China 5 (4), 510–517.
Nakamura, Y., Matsukawa, T., 1987. Vortex excitation of rectangular cylinders with a long side normal to the flow. J. Fluid Mech. 180, 171–191.
Nakamura, Y., Nakashima, M., 1986. Vortex excitation of prisms with elongated rectangular, H and ⊢ cross-sections. J. Fluid Mech. 163, 149–169.
Nakamura, Y., Ohya, Y., Tsuruta, H., 1991. Experiments on vortex shedding from flat plates with square leading and trailing edges. J. Fluid Mech. 222, 437–447.
Naudascher, E., Wang, Y., 1993. Flow-induced vibrations of prismatic bodies and grids of prisms. J. Fluids Struct. 7, 341–373.
Nicese, B., 2021. Influence of Cross-Section Details on Vortex-Induced Vibrations of Bridge Decks: Experiments and Modeling. University of Florence, Florence, Italy. Ph.D. Thesis.
Owen, J.S., Vann, A.M., Davies, J.P., Blakeborough, A., 1996. The prototype testing of Kessock Bridge: response to vortex shedding. J. Wind Eng. Ind. Aerodyn. 60, 91–108.
Parkinson, G.V., Wawzonek, M.A., 1981. Some considerations of combined effects of galloping and vortex resonance. J. Wind Eng. Ind. Aerodyn. 8, 135–143.
Ricciardelli, F., de Grenet, E.T., Hangan, H., 2002. Pressure distribution, aerodynamic forces and dynamic response of box bridge sections. J. Wind Eng. Ind. Aerodyn. 90 (10), 1135–1150.
Rockwell, D., Naudascher, E., 1978. Self-sustaining oscillations of flow past cavities. J. Fluids Eng. 100, 152–165.
Sarwar, M.W., Ishihara, T., 2010. Numerical study on suppression of vortex-induced vibrations of box girder bridge section by aerodynamic countermeasures. J. Wind Eng. Ind. Aerodyn. 98, 701–711.
Schewe, G., 1989. Nonlinear flow-induced resonances of an H-shaped section. J. Fluids Struct. 3 (4), 327–348.
Schewe, G., Larsen, A., 1998. Reynolds number e¤ects in the flow around a blu¤ bridge deck cross section. J. Wind Eng. Ind. Aerodyn. 74-76, 829–838.
Seo, J.W., Kim, H.K., Park, J., Kim, K.T., Kim, G.N., 2013. Interference effect on vortex-induced vibration in a parallel twin cable-stayed bridge. J. Wind Eng. Ind. Aerodyn. 116, 7–20.
Shiraishi, N., Matsumoto, M., 1983. On classification of vortex-induced oscillation and its application for bridge structures. J. Wind Eng. Ind. Aerodyn. 14, 419–430.
Stokes, A.N., Welsh, M.C., 1986. Flow-resonant sound interaction in a duct containing a plate, II: square leading edge. J. Sound Vib. 104, 55–73.
Sun, Y., Li, M., Li, M., Liao, H., 2019. Spanwise correlation of vortex-induced forces on typical bluff bodies. J. Wind Eng. Ind. Aerodyn. 189, 186–197.
Tamura, Y., Shimada, K., 1987. A mathematical model for the transverse oscillations of square cylinders. In: Proceedings of the 1st International Conference on Flow Induced Vibrations. Bowness-on-Windermere, UK, pp. 267–276.
Wang, X., Xu, F., Zhang, Z., Wang, Y., Zhang, M., 2023. Numerical explorations of the vortex-induced vibration of a streamlined box girder with water-filled barriers. J. Wind Eng. Ind. Aerodyn. 240, 105496.
Wang, Y., Chen, X., Li, Y., 2020. Nonlinear self-excited forces and aerodynamic damping associated with vortex-induced vibration and flutter of long span bridges. J. Wind Eng. Ind. Aerodyn. 204, 104207.
Weber, F., Distl, J., Maślanka, M., 2013. Semi-active TMD concept for Volgograd Bridge. In: Proceedings of the 31st IMAC, A Conference on Structural Dynamics, pp. 79–88.
Yan, Y., Yagi, T., Noguchi, K., Ito, Y., Shimada, R., 2022. Effects of Handrail Details on Vortex-Induced Vibration for a Box-Girder Bridge. J. Bridge Eng. 27 (3), 04021114.
Zhu, L.D., Meng, X.L., Guo, Z.S., 2013. Nonlinear mathematical model of vortex-induced vertical force on a flat closed-box bridge deck. J. Wind Eng. Ind. Aerodyn. 122, 69–82.